SAMARA

University of Maryland Undergraduate Design Team

2020 VFS Design Competition Sponsored by Leonardo Helicopters

A revolutionary electric vertical take-off and landing vehicle based on Leonardo da Vinci's original Aerial Screw designs.

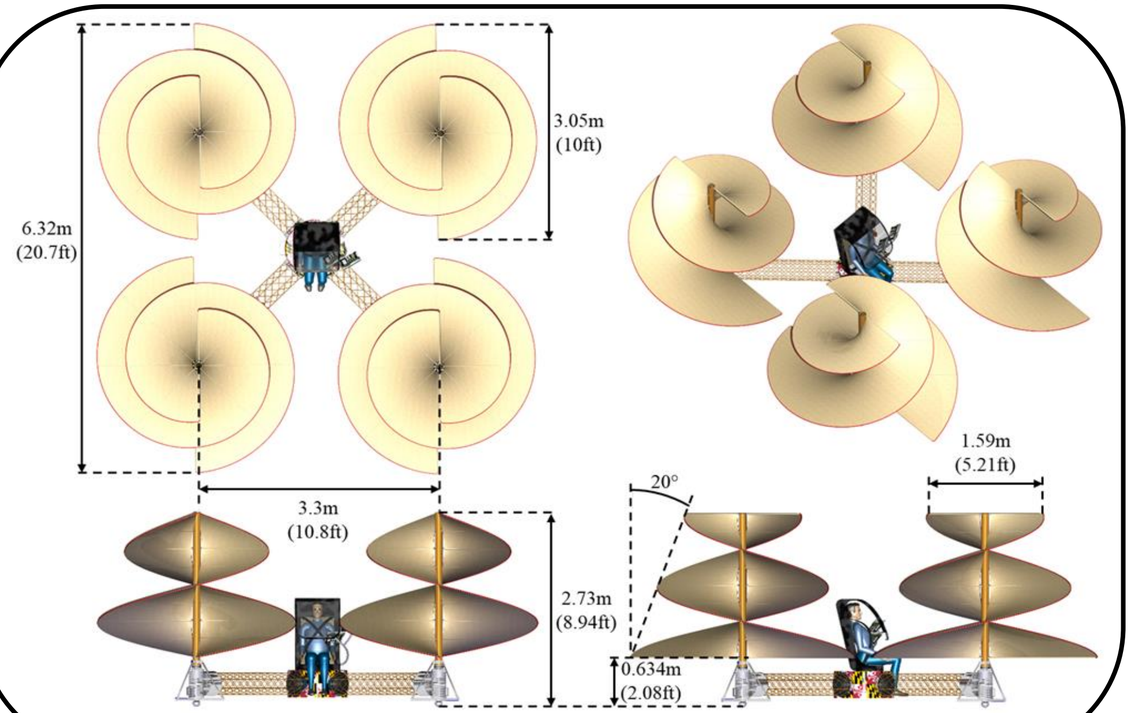

Samara Three and Isometric View

Efficient Airscrew developed after Extensive Testing and CFD

Experimental Testing with Smoke Generator

- Leading edge vortex discovered (DaVi Vortex)
- Extensive experimental testing
- Smoke generator flow visualization
- CFD Analysis

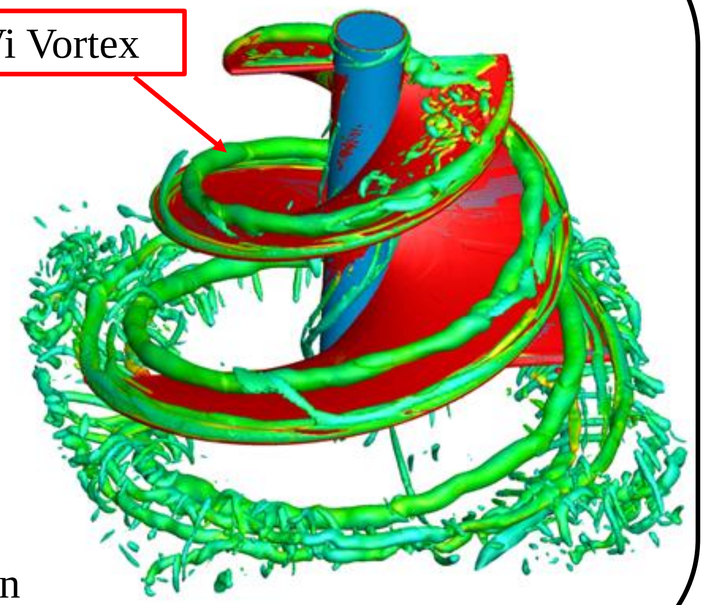

CFD Vortex Analysis

Compact Powertrain and Landing Gear Assembly

- Sorbothane foot
- Rubber shock absorbers
- Compact casing to house powertrain
- Easy battery access

Landing Gear and Powertrain Casing

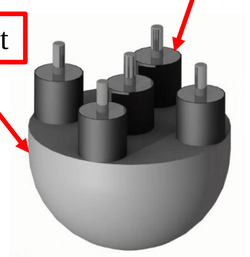

Historically Inspired Aerial Screw

- Single bladed concentric screws to reduce vibrations
- Dacron fabric covering spars
- Carbon fiber spars
- 20° initial pitch angle
- Tapered radius follows da Vinci's aesthetics

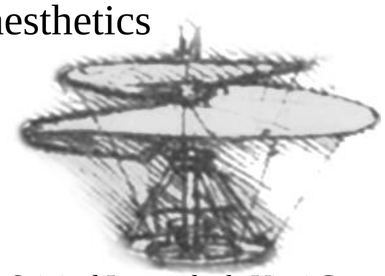

Original Leonardo da Vinci Concept

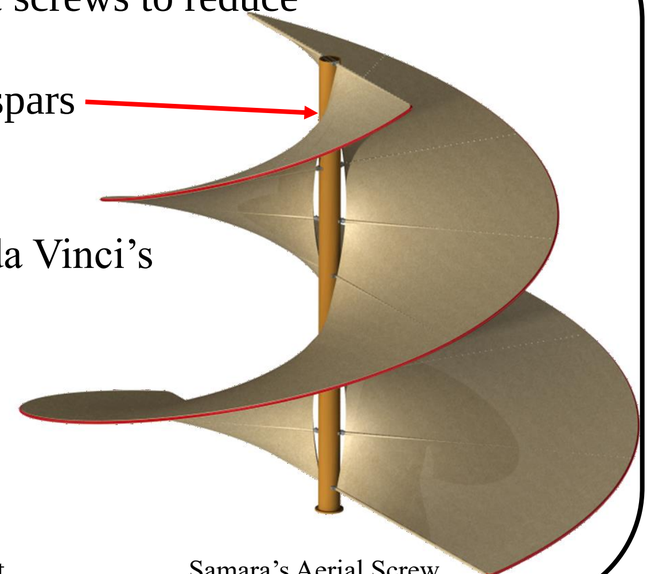

Samara's Aerial Screw

Ultralight Airframe

- Carbon fiber OctaTruss Arms
- Dacron fabric rotor
- Carbon fiber cockpit frame
- Aluminum landing gear

OctaTruss Design

Key Technical Specs:

- Payload: 60 kg (1 person)
- GTOW: 290 kg
- Max Rotor Radius: 1.59 m
- Installed Power: 60 kW
- Disk Loading: 10.8 kg/m^2
- Endurance: 3 min. 3 sec.

Samara

37th Annual VFS Student Design Competition

Leonardo's Aerial Screw: 500 Years Later

Sponsored by Leonardo Helicopters

Alfred Gessow Rotorcraft Center
Department of Aerospace Engineering
University of Maryland
College Park, MD 20742 U.S.A.

UNIVERSITY OF MARYLAND

Alfred Gessow Rotorcraft Center
Department of Aerospace Engineering
University of Maryland
College Park, MD 20742 U.S.A.

Austin McClelland
Undergraduate Student
amcclell@terpmail.umd.edu

Blaise Martineau
Undergraduate Student
blaisem8@terpmail.umd.edu

Charlie Flanagan
Undergraduate Student
cflanaga@terpmail.umd.edu

Christopher Savage
Undergraduate Student
csavage4@terpmail.umd.edu

James Lynott
Undergraduate Student
jimmylynott@gmail.com

Julia Mittelstaedt
Undergraduate Student
jul.mittelstaedt8@gmail.com

Nathan Lloyd
Undergraduate Student (Team Captain)
nlloyd@umd.edu

Nick VanZelst
Undergraduate Student
nrvanzelst@gmail.com

Seong Yun
Undergraduate Student
syun9515@terpmail.umd.edu

Dr. Inderjit Chopra
Faculty Advisor
chopra@umd.edu

Dr. James D. Baeder
Faculty Advisor
baeder@umd.edu

Dr. Vengalattore Nagaraj
Faculty Advisor
vnagaraj@umd.com

The students listed above will receive credit for the course ENAE 481 and ENAE 482: Helicopter Design.

Alfred Gessow Rotorcraft Center
Department of Aerospace Engineering
University of Maryland
College Park, MD 20742 U.S.A.

To Vertical Flight Society:

The members of the University of Maryland Undergraduate Student Design Team hereby grant VFS full permission to distribute the enclosed Executive Summary and Final Proposal for the 37th Annual Design Competition as they see fit.

The UMD Undergraduate Design Team

Note to VFS Regarding Report Organization

The members of the University of Maryland Undergraduate Student Design Team acknowledge the Vertical Flight Society's request for this report's chapter layout and contents. However, it was necessary for the contents of this report to follow an alternative structure. This rearrangement improves readability and succinctness. All required material is still included. Below is a reference table mapping out these changes.

VFS Mandated Chapters	**Corresponding Report Chapters**
Configuration Trade Off Analysis	[2]
Selected Concept Sizing and Description	[3]
Overall Geometry and Aesthetics	[6], [6.1], [6.2], [6.3], [6.4]
Aerodynamics	[4], [4.5], [4.6], [5]
Structures and Materials	[6]
Power and Energy	[7]
Rotor	[4], [6.1]
Controls and Piloting	[8]
Concept Validation	[4]
Capability, Performance, and Requirement Analysis	[3], [4], [4.6], [5.12] [9]

Acknowledgements

The design team wishes to acknowledge the following people for their invaluable discussion, guidance, and support throughout the course of this project.

University of Maryland Faculty:

Dr. Vengalattore T Nagaraj – Research Scientist, Department of Aerospace Engineering, University of Maryland, College Park

Dr. Inderjit Chopra – Distinguished Professor, Department of Aerospace Engineering,

University of Maryland, College Park

Dr. James Baeder – Professor, Department of Aerospace Engineering, University of Maryland, College Park

Alfred Gessow Rotorcraft Center Students:

Ian Bahr

Seyhan Gul

Yong Su Jung

Brandyn Phillips

Jordan Schmidt

Contents

List of Figures ..... **v**

List of Tables ..... **ix**

1 Introduction **1**
1.1 RFP Aesthetic and Geometry Compliance Summary 2
1.2 Mission Profile 3

2 Configuration Trade-Off Analysis **3**
2.1 Design Drivers 3
2.1.1 Analytical Hierarchy Process (AHP) 4
2.2 Configurations Considered 5
2.2.1 Pugh Matrix 6

3 Selected Concept Sizing and Description **7**
3.1 Preliminary Vehicle Sizing 7
3.1.1 Description of Sizing Algorithm 7
3.1.2 Disk Loading Parametric Study 8

4 Concept Validation **8**
4.1 Evolution of Design 8
4.2 Testing Setup and Procedure 8
4.3 Test Equipment 10
4.3.1 Flow Visualization 10
4.3.2 Relating Electric and Mechanical Power 11
4.4 Results 11
4.4.1 Stage 1: Initial Testing: FM = 0.05 11
4.4.2 Stage 2: Slotted Blades: FM = 0.05 12
4.4.3 Stage 3: Single Turn Aerial Screws 13
4.4.4 Stage 4: Double-Turn, Single Surface, Concentric Aerial Screw Tests: FM = 0.075 15
4.4.5 Stage 5: Half-Turn Aerial Screws (effect of root pitch angle): FM = 0.45 (H=75mm), FM = 0.04 (H = 50mm) (2500 RPM) 15
4.4.6 Stage 6: Tapered, Single Surface, Concentric Aerial Screw: FM = 0.38 17
4.5 2D CFD 18
4.6 3D CFD 18
4.6.1 Flow Visualization 19

5 Aerodynamics **20**
5.1 Modeling High Solidity Rotors 20
5.1.1 Scale Model Testing 20
5.1.2 CFD 21

6 Structure Geometry, Materials, and Aesthetics **21**

6.1 Rotor 21
6.1.1 Rotor Structural Analysis 22
6.2 Landing Gear 22
6.2.1 Landing Gear Structural Analysis 23
6.3 OctaTruss Airframe Structure 24
6.3.1 OctaTruss Structural Analysis 25
6.4 Cockpit 26
6.4.1 Cockpit Structural Analysis 27
6.5 OctraTruss Mounting Bolts to Cockpit Structural Analysis 28
6.6 Human Accessibility Factor 29
6.7 Demonstrator Manufacturing and Feasibility 29
6.8 Cost of Materials 30

7 Power and Energy 31
7.1 Powertrain Selection 31
7.2 Power Requirements 31
7.3 Powertrain Components 31
7.3.1 Motor 31
7.3.2 Battery 33
7.3.3 Electronic Speed Controller 34
7.3.4 Standard Operating Conditions 34
7.3.5 Powertrain Circuit 35

8 Controls and Piloting 36
8.1 Mission Avionics Requirements 36
8.1.1 Cockpit Display and Controls 39

9 Capability, Performance, and Requirement Compliance 40

Bibliography 41

List of Figures

Figure 1.1: Historical sketch of Leonardo da Vinci's Aerial Screw [13] 1
Figure 1.2: Mission profile 3
Figure 2.1: Non-dimensionalized weights and ranking of configuration selection drivers 5
Figure 2.2: Configurations considered 5
Figure 3.1: Flowchart for the vehicle sizing procedure 7
Figure 3.2: Disk loading parametric study 8
Figure 4.1: TS1 9
Figure 4.2: TS2 9
Figure 4.3: Fog machine used for flow visualization 10
Figure 4.4: Relationship between shaft power and electrical power 11
Figure 4.5: Flow visualization of $\sigma = 0.24$ commercial rotor 12
Figure 4.6: Rotor profiles for initial testing 12
Figure 4.7: Flow visualization of $\sigma = 0.25$, $\theta = 10°$ rotor 12
Figure 4.8: Flow visualization of $\sigma = 0.25$, $\theta = 10°$ rotor 12
Figure 4.9: Slotted-half-solitity blade: 12
Figure 4.10: Coefficient of thrust vs. RPM of slotted rotor and well performing rotors from Stage 1 13
Figure 4.11: Coefficient of power vs. RPM of slotted rotor and well performing rotors from Stage 1 13
Figure 4.12: Flow visualization of $\sigma = 0.25$, $\theta_{root} = \theta_{tip} = 10°$ rotor 13
Figure 4.13: Single-turn Aerial Screw Height = 100 mm 13
Figure 4.14: Single-turn Aerial Screw with slots Height = 100 mm 13
Figure 4.15: FM vs. RPM of a Double-Turn, Single Surface, Concentric Aerial Screw 14
Figure 4.16: C_T and C_P vs. RPM of 14
Figure 4.17: Still images from a video showing inherent vibrations of a Single-Turn Aerial Screw 14
Figure 4.18: Flow visualization of Single-Turn Aerial Screw 14
Figure 4.19: Flow visualization Double-Turn, Single Surface, Concentric Aerial Screw 14
Figure 4.20: Double-Turn, Single Surface, Concentric Aerial Screw 15
Figure 4.21: (From left to right) 2 Half-Turn Aerial Screws and a Double-Turn, Single Surface, Concentric Aerial Screw 15
Figure 4.22: FM vs. RPM of Half-Turn Aerial Screws and Double-Turn, Single Surface, Concentric Aerial Screw 15

Figure 4.23: Flow visualization for half-turn Aerial Screw with 75 mm height, θroot = 67.3° 16

Figure 4.24: C_P vs. RPM of half-turn Aerial Screws and Double-Turn, Single Surface, Concentric Aerial Screw 16

Figure 4.25: Flow visualization for half-turn Aerial Screw with 50 mm height, θ_{root} = 57.8° 16

Figure 4.26: Flow Visualization for Double-Turn, Single Surface, Concentric Aerial Screw Aerial Screw, θ_{root} = 57.8° 16

Figure 4.27: C_T vs. RPM of half-turn Aerial Screws and Double-Turn, Single Surface, Concentric Aerial Screw 16

Figure 4.28: Tapered, Single Surface, Concentric Aerial Screw 17

Figure 4.29: Flow visualization of Tapered, Single Surface, Concentric Aerial Screw 17

Figure 4.30: FM as a function of RPM of Tapered, Single Surface, Concentric Aerial Screw rotating "forwards" and "backwards" 17

Figure 4.31: C_T vs. RPM of Tapered, Single Surface, Concentric Aerial Screw rotating "fowards" and "backwards" 17

Figure 4.32: C_P vs. RPM of Tapered, Single Surface, Concentric Aerial Screw rotating "fowards" and "backwards" 17

Figure 4.33: Top down view of surface mesh 18

Figure 4.34: Isometric view of surface mesh 18

Figure 4.35: Full model view with strand layers (in red), nested off body background mesh (in blue), and uniform grid spacing (in green) 18

Figure 4.36: Close up view of rotor tip and surrounging strand layers (in red), and nested off body background mesh (in green) 18

Figure 4.37: Uniform grid spacing (in blue) around model in center of figure 18

Figure 4.38: Streamlines of the rotor from the side 19

Figure 4.39: Visualization of vorticies on the final design 20

Figure 4.40: Interaction between tip vortex and DaVi vortex 20

Figure 5.1: 3D printed rotors used in scale model testing 20

Figure 5.2: Flow visualization performed for many test cases 20

Figure 6.1: Rotor with transparent surface 21

Figure 6.2: Top down view of rotor and some of its components 22

Figure 6.3: Rotor spar stress response 22

Figure 6.4: Rotor spar total deformation under point load 22

Figure 6.5: Landing gear assembly 22

Figure 6.6: Landing gear without powertrain enclosure 23
Figure 6.7: Sorbothane impulse response 23
Figure 6.8: Sorbothane transmissibility at resonance 23
Figure 6.9: Sorbothane landing gear shock absorber stress response 24
Figure 6.10: Sorbothane landing gear shock absorber deformation response 24
Figure 6.11: Stabilization I-beam stress response 24
Figure 6.12: Stabilization I-beam deformation under multiple point loads 24
Figure 6.13: OctaTruss 24
Figure 6.14: Diamond bay cross section 25
Figure 6.15: "X" bay cross section 25
Figure 6.16: Section view of OctaTruss structure 25
Figure 6.17: OctaTruss tip load deflection 26
Figure 6.18: OctaTruss equivalent stress response 26
Figure 6.19: Cockpit 26
Figure 6.20: Cockpit stress response 27
Figure 6.21: Cockpit frame deformation 27
Figure 6.22: Windshield stress response due to bird strike 27
Figure 6.23: Windshield deformation due to bird strike 27
Figure 6.24: Shear stress respose 29
Figure 6.25: Tensile stress respose 29
Figure 7.1: Weight estimates of various powertrains 31
Figure 7.2: EMRAX 188 combined cooling efficiency chart 31
Figure 7.3: Maximum RPM as a function of continuous power 32
Figure 7.4: Kv as a function of voltage of EMRAX motors 32
Figure 7.5: Kt vs. current of EMRAX motors 32
Figure 7.6: Specific power vs. mass of EMRAX motors 33
Figure 7.7: EMRAX 188 34
Figure 7.8: MaxAmps Li-Po 44.4V 9000XL 34
Figure 7.9: Mauch HS-200-HV 34
Figure 7.10: AMPX ESC 200A (12s-24s) HV 34
Figure 7.11: Wiring diagram of vehicle powertrain 35

Figure 7.12: Circuit associated with each rotor 35
Figure 8.1: Samara RPM control diagram 36
Figure 8.2: Control system concept flow chart 36
Figure 8.3: Onboard avionics 36
Figure 8.4: Top-down view of pilot sightlines green regions: unobstructed FOV yellow regions: FOV obstructed by rotors gray regions: FOV obstructed by cockpit 38
Figure 8.5: Pilot point-of-view FOV, 18% is unobstructed, cameras increase pilot FOV by over 500% 38
Figure 8.6: Cockpit Display and Controls 39

List of Tables

Table 1.1: Overview of Samara 2
Table 2.1: Non-dimensionalized AHP matrix of configuration selection drivers 4
Table 2.2: Pugh matrix 6
Table 4.1: Evolution of scale model rotor characteristics 9
Table 4.2 : CFD results for R_{max} = 0.075m (2.95in) 19
Table 4.3: CFD results for R_{max} = 1.518m (3.28ft) 19
Table 6.1: Motor, Gearbox, and Landing Gear Assembly Dimenstions 28
Table 6.2: Summary of vehicle specifications 28
Table 6.3: Estimate cost 30
Table 7.1: Kt and Kv Values for Operating Voltages 33
Table 7.2: Comparison of Battery Weights Required to Meet Vehicle Specifications 34
Table 7.3: Motor: 16.6kW Scaled EMRAX Motor 34
Table 7.4: ESC: AMPX ESC 200A (12s-24s) HV 35
Table 7.5: Battery: MaxAmps Li-Po 44.4V 9000XL 35
Table 8.1: Avionic component description 38
Table 9.1: *Samara* RFP Requirements and Compliance 40
Table 9.2: Documentation Requirements and Compliance 40

Three-View of Samara

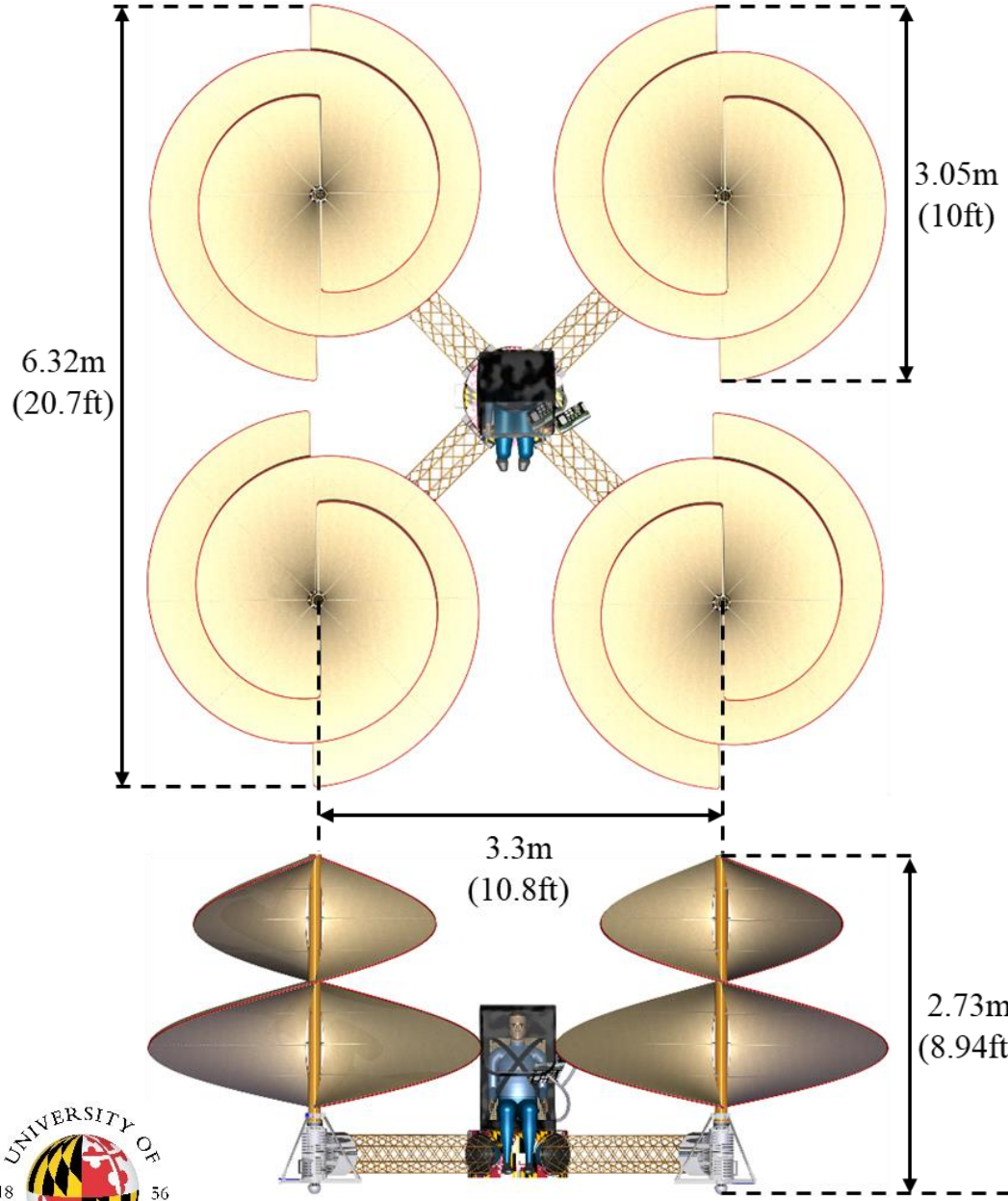

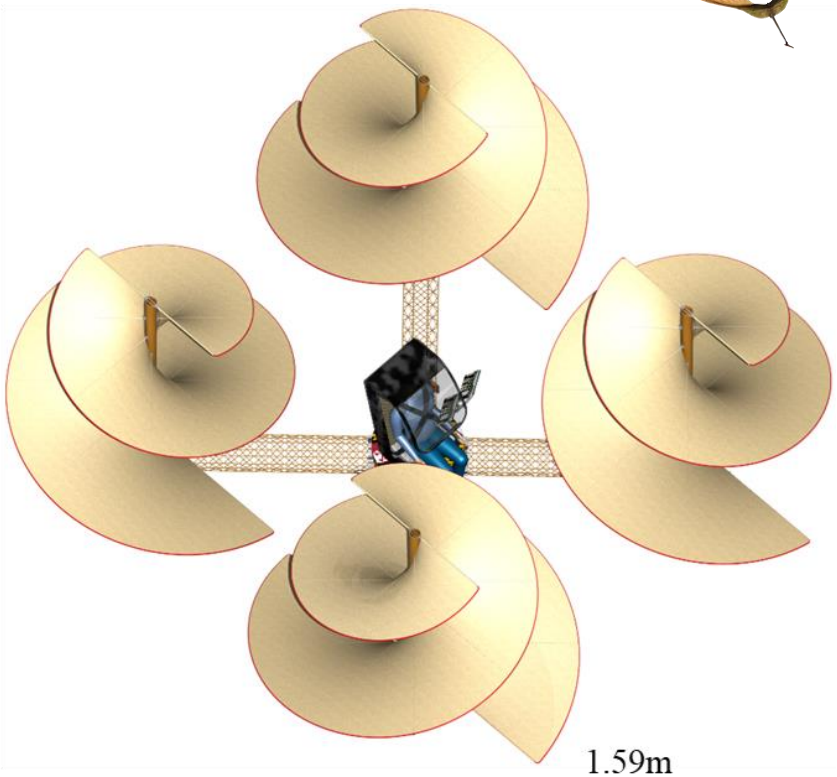

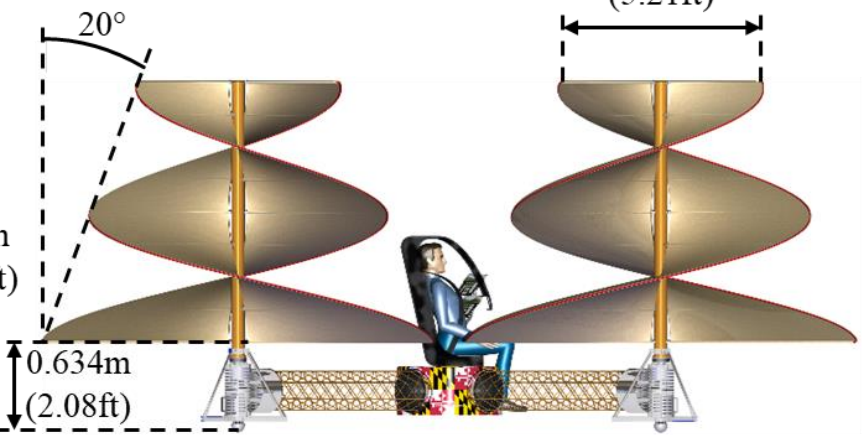

UNIVERSITY OF MARYLAND 18 56

1 Introduction

Throughout history, there have been extraordinary individuals that push the boundaries of what humankind considers impossible. They dream big, challenge what is considered fact, and pursue change for the sake of science and humanity. They follow different endeavors: they are artists, engineers, scientists, philosophers, doctors, and scholars. Leonardo da Vinci was all of these and more [1].

Leonardo da Vinci was born in 1452 and contributed much to society in the fields of art and science. He documented many of his thoughts on nature, anatomy, physics, and complex machinery. In his journals, he designed machines centuries ahead of his time. Machines such as the bicycle, submarine, military tank, and helicopter [1].

da Vinci named his helicopter the Aerial Screw. The Vertical Flight Society (VFS) identifies this as "the first human-carrying vertical take-off and landing machine ever designed" [2]. It was conceived around 1483 [3] but was not constructed until 2010 [4]. It appeared on an episode of The Discovery Channel's television series "Doing DaVinci" [4]. Unfortunately, this construction was more of a novelty. It was built to Leonardo da Vinci's specifications, but there was no attempt to understand the physics behind it, or to find any advantages of a rotorcraft with such a unique design. The aerospace company, Leonardo Helicopters, claims,

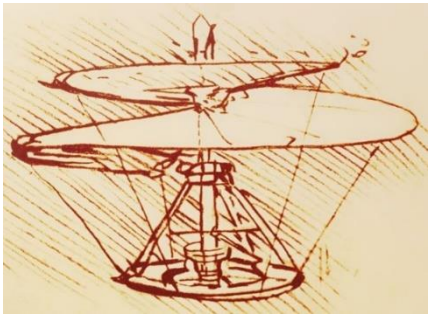

Figure 1.1: Historical sketch of Leonardo da Vinci's Aerial Screw [13]

> *The actual pros and cons of the Aerial Screw are often quoted but have not been analyzed extensively, nor has a possible working application been studied, leaving a gap in the technical understanding of the significance of the invention* [2].

In response to the 2020 VFS student design competition Request for Proposal (RFP), the Undergraduate Design team of the Alfred Gessow Rotorcraft Center, at the University of Maryland, proudly presents *Samara*: an autonomous, ultralight, and electric quadrotor with da Vinci inspired, high solidity, Aerial Screw rotors. *Samara* closes a significant gap in understanding in the realm of high solidity rotors. *Samara* is named after one of Leonardo da Vinci's inspirations for the Aerial Screw: maple tree seeds falling in late spring [5]. *Samara* is also the first scientifically proven reinvention of the Aerial Screw. After over five centuries from its inception as a hypothesis, within this milestone project, da Vinci's Aerial Screw has been brought to life and its merits quantified.

The tools necessary to design *Samara* and the resulting concepts were developed in a hands-on environment. By testing scale models, conducting detailed Computational Fluid Dynamics analyses (CFD), and consulting distinguished professors, the *Samara* team accumulated valuable data and developed mathematical models to justify *Samara*'s performance specifications. An overview of *Samara's* features is given in Table 1.1.

1.1 RFP Aesthetic and Geometry Compliance Summary

The RFP places significant emphasis on the aesthetics and geometry of da Vinci's original design. An Aerial Screw is defined by the RFP as a "single-blade rotor with solidity equal or greater than one with a continuous surface" [2]. While the RFP requests a "single-bladed rotor," the goal of the competition is "to design a VTOL vehicle based on Leonardo's Aerial Screw concept, studying and demonstrating the consistency of its physics and potential feasibility" [2]. *Samara* fulfills this goal and demonstrates a deep understanding of the Aerial Screw concept.

All efforts were made to adhere to the requested geometric requirements while also considering mission performance requirements. Testing revealed significant challenges to the Aerial Screw design. Both a mass and an aerodynamic imbalance are inherent to an Aerial Screw, producing significant vibrations that threaten the structural integrity of the rotor and the vehicle if ignored. Although there are potential methods for solving the mass imbalance problem, no configuration was found that could efficiently and simultaneously solve both imbalances for an Aerial Screw.

Table 1.1: Overview of Samara

Features	**Summary**
Rotor design maintains the original aesthetic of Leonardo da Vinci's Aerial Screw	Rotor tapers inward as the surface goes upward. A fabric is used for the rotor surfaces. Specialized single surface concentric Aerial Screw minimizes vibration
Dacron rotor surfaces	This high strength material is used for ultralight aircraft. It has a high strength to weight ratio [6].
Computational Fluid Dynamic simulation and scale model testing verification of rotor performance	The experimental data from the scale model tests were scaled to full rotor dimensions. This data was verified using Computational Fluid Dynamics (Chapter 4.6).
Ultralight frame	*Samara's* frame is a based off the Isotruss patented design and is optimized for its mission requirements. It has 2 times the strength of steel [7].
Simple onsite assembly and ground maintenance	*Samara* may be disassembled for transport and reassembled onsite. This also allows for easy onsite repairs of all components.
Fully electric powertrain	A fully electric powertrain was designed to reduce the weight and complexity of *Samara*.
Quadcopter configuration with full autonomous flight control capability	Four rotors increase flight stability. Mission profiles may be programmed into the onboard flight controller and executed in full autonomy, or the pilot can take control.

Samara's single surface concentric Aerial Screw addresses both imbalances while performing at a level that exceeds the mission's requirements (see Chapter 9). Each single surface concentric Aerial Screw has a solidity greater than 1.0 and adheres to the spirit and intention of da Vinci's original vehicle (see Table 1.1).

The mission profile mandated in the RFP [2] (fully defined in Chapter 1.2) and appears simple. A 70s endurance and 20m (66ft) range minimum performance is rudimentary for conventional rotorcraft. However, in an unexplored field of aeronautical engineering, it is not so straightforward. The concepts developed over the last two and a half centuries provide solely intuition on how to engineer an Aerial Screw.

1.2 Mission Profile

The RFP provides a detailed problem statement for the design of the vehicle and its mission profile [2]. *Samara* adheres to both the design and operational requirements within the RFP. These requirements and the mission profile are as follows.

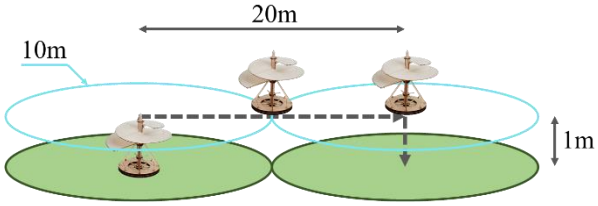

Figure 1.2: Mission profile

The vehicle must rely on one or more single-blade rotors with solidity equal or greater than 1.0 with a continuous surface for lift and thrust. It also must be capable of carrying a person weighing at least 60kg (132lb). The vehicle must takeoff vertically and hold the position for at least 5s within a 10m (33ft) radius of the takeoff spot. It must fly for at least 60s, covering at least 20m (66ft) of distance at an altitude of at least 1m (3.3ft). Finally, it must land vertically, after holding the position for 5s within a 10m (33ft) radius from landing spot. An illustration of the mission profile is shown in Figure 1.2.

2 Configuration Trade-Off Analysis

To determine design driving factors, an Analytic Hierarchy Process (AHP) was undertaken and subsequent Pugh matrices were constructed. This resulted in the development of an unbiased and quantitative way to evaluate design criteria and features. After analyzing numerous potential design factors, the nine most critical considerations were chosen to create a concise AHP matrix (Table 1.1). The non-dimensionalized weights produced by the AHP matrix are illustrated in Figure 2.1.

2.1 Design Drivers

Aesthetic (physical resemblance to da Vinci's Aerial Screw): The spirit of the RFP is to design an aircraft that closely resembles an Aerial Screw. Distinguishing characteristics of da Vinci's invention are the main vertical shaft, continuous fabric surfaces, and vertical tapered rotor.

Weight: Minimizing Gross Take-Off Weight (GTOW) is tied to several performance metrics such as powertrain, structure, and rotor performance.

Cost: Evaluation of cost should factor into any practical engineering project. Budget considerations constrict material, manufacturing, and hardware decisions to affordable Commercial Off-The-Shelf (COTS) products. This enables the vehicle to proceed past the design phase, and into the manufacturing phase, with a cost justifiable by the project's significance and customer budget.

Range/ Endurance (maximum distance and time the vehicle can travel): Range and endurance minimums are mandated by the RFP. Despite these values being small, by industry standards, it is important to strive to design a vehicle that can exceed its performance requirements.

Stability/ Controllability (pilot workload): The RFP states the aircraft must not drift outside of a specified radius while in hover – dismissing potential environmental factors. However, rotor stability and controls to counteract possible drift still warrant examination. Control considerations examine the maneuverability of the vehicle configuration and dictate flight control software and hardware necessity.

Safety: Pilot, spectator, and property safety is a necessary consideration for all engineering endeavors. This means ensuring a safe cockpit environment, vehicle structural integrity, maneuverability, and mitigating harm in the event of a crash.

Noise: Acoustics become a factor for all manned aircraft or any aircraft that flies in or around populated areas. Vehicle operation cannot obstruct pilot or ground communication.

Durability: The short range and endurance requirement indicate that *Samara* undergo many take-off and landing cycles. A human payload also demands higher standards of durability for safety. Durability is closely tied to weight, so it is important to consider trade-offs between lowering the GTOW and maintaining a proper safety factor.

Hover Capability: The capability to successfully lift off the ground and maintain hover is critical to *Samara's* mission. As a low altitude vehicle with limited range and endurance, overcoming the aerodynamic challenges associated with an Aerial Screw as the primary lift device is the crux of the mission.

2.1.1 Analytical Hierarchy Process (AHP)

Table 2.1: Non-dimensionalized AHP matrix of configuration selection drivers

	Aesthetic	Weight	Cost	Range/ Endurance	Stability/ Controllability	Safety of Crew	Noise	Durability	Hover Capability	Normalized Priority Vector
Aesthetic	0.07	0.35	0.22	0.04	0.04	0.28	0.14	0.05	0.07	0.139
Weight	0.01	0.07	0.22	0.12	0.12	0.09	0.14	0.25	0.07	0.121
Cost	0.01	0.01	0.03	0.04	0.04	0.02	0.10	0.05	0.07	0.040
Range/ Endurance	0.22	0.07	0.09	0.12	0.12	0.09	0.14	0.15	0.11	0.124
Stability/ Controllability	0.22	0.07	0.09	0.12	0.12	0.09	0.14	0.15	0.11	0.124
Safety of Crew	0.02	0.07	0.16	0.12	0.12	0.09	0.10	0.15	0.11	0.105
Noise	0.01	0.01	0.01	0.02	0.02	0.02	0.02	0.01	0.05	0.017
Durability	0.07	0.01	0.03	0.04	0.04	0.03	0.10	0.05	0.11	0.054
Hover Capability	0.36	0.35	0.16	0.37	0.37	0.28	0.14	0.15	0.33	0.277

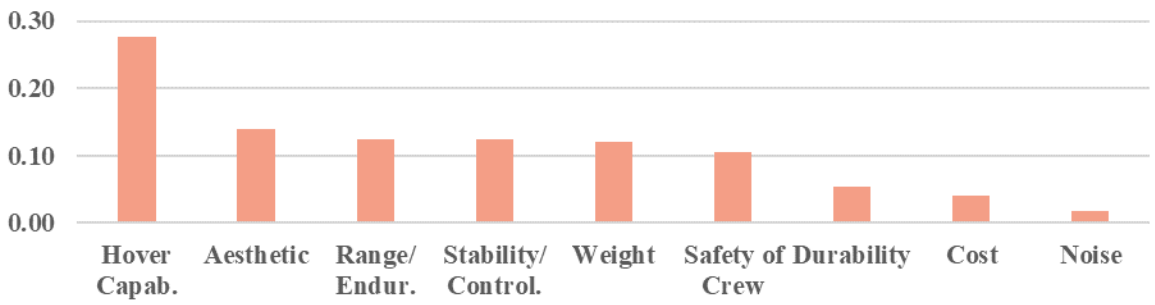

Figure 2.1: Non-dimensionalized weights and ranking of configuration selection drivers

2.2 Configurations Considered

Rotor and structural considerations were discussed at length to determine how the Aerial Screw design would function as a human transport vehicle. Without an anti-torque device, da Vinci's design is impossible to control as he had envisioned. All rotorcraft require an anti-torque device to counteract the torque imparted onto the vehicle structure by the main rotor. This is necessary for stability and control. Two popular anti-torque design configurations are tail rotors and paired counter-rotating main rotors. To determine which configuration was most compatible with Aerial Screw rotors, different traditional rotorcraft configurations were considered in terms of the design drivers. Each configuration was compared as if they all incorporated Aerial Screws for their primary source of lift.

A brief description of each configuration and their advantages and disadvantages compared to a single main rotor are listed below (SMR). Additionally, images of each configuration are shown in Figure 2.2.

SMR: This is the most common helicopter configuration. A SMR helicopter requires an anti-torque device – typically a tail rotor – which uses power from the same power plant. Reduced complexity and cost are the SMR's typical advantage. The disadvantages are, not all vehicle power is used for lift, and its controllability may be challenging when utilizing an Aerial Screw. Without separate blades and swashplate, it is impossible to control blade pitch cyclically and collectively.

Tandem: This configuration has two main rotors placed at the front and the rear of the helicopter. The counter-rotating rotors provide anti-torque; therefore, the entirety of powerplant is used for lift. This configuration is advantageous for larger helicopters with heavier payloads. Tandem rotors also allow for a greater range for the center of gravity, meaning they can accommodate wider payloads with less placement restrictions. This advantage is not pertinent since the sole payload is a stationary passenger. A tandem rotor would also be difficult to control without a swashplate and would present stability problems along the body of the vehicle's axis.

Figure 2.2: Configurations considered

Coaxial: This configuration consists of two counter-rotating main rotors along the same axis of rotation. Like the tandem configuration, these rotors provide anti-torque, therefore the power plant is used entirely for lifting rotors. This configuration allows for greater maneuverability at low speeds. However, this design is also not practical for tall rotors without swashplates. In addition to stability considerations, controllability would be hindered, so any typical maneuverability advantage is negated.

Quadcopter: A quadcopter uses four main rotors with two rotating clockwise and two counterclockwise for anti-torque. All the power is used to provide lift. Quadcopters have excellent maneuverability at low speeds. The greatest advantage is the ability to control the aircraft without requiring a swashplate. Varying the RPM of each rotor creates a difference in lift to pitch the aircraft in any direction.

Table 2.2: Pugh matrix

	Weight	SMR	Coaxial	Tandem	Quadcopter	Ducted Fan
Aesthetic	0.139	0	-1	-2	-2	-1
Weight	0.121	0	-2	-1	1	-4
Cost	0.040	0	-1	0	2	-4
Range/ Endurance	0.124	0	0	1	4	1
Stability/ Controllability	0.124	0	0	2	4	1
Safety of Crew	0.105	0	-1	0	0	-2
Noise	0.017	0	0	0	0	1
Durability	0.054	0	-2	-1	1	-2
Hover Capability	0.277	0	0	0	2	1
	Score	0.00	-0.63	-0.08	1.52	-0.56

Single Ducted Fan: Ducted fans have been found to have lower hover power requirements than open rotors to produce the same amount of thrust [3]. It is possible to have a single rotor in this configuration using control surfaces within the downwash for counter torque and maneuverability. However, the advantages diminish for larger diameter rotors. In addition to a restrictive radius necessary for the Aerial Screw, the duct would have to be tall enough to fit the screw, adding additional weight. The weight added would be too restrictive on hover performance to be a successful design.

2.2.1 Pugh Matrix

A Pugh matrix is used to facilitate the design and decision-making process: a method for comparing of several design candidates. The result is the selection of a configuration that best meets the design criteria.

Table 2.2 shows the Pugh matrix constructed to rank the configurations based on the selected design drivers. Each configuration was compared against the SMR. A grading scale of integers ranging from -4 (much worse) to 4 (much better) was used. The grades were assigned following discussion regarding the pros and cons of each configuration generally, and then in relation to the Aerial Screw design. The scores were given independent of design driver importance for each category. Afterwards, the scores were weighted by the values produced from the AHP matrix. The quadcopter configuration was the clear choice at the conclusion of the trade-off analysis. The alternative configurations, in order of most to least applicable, are SMR, Tandem, Ducted Fan, and Coaxial (see the last row of Table 2.2).

3 Selected Concept Sizing and Description

The focus of *Samara's* design was to achieve lift from a rotor that many thought was impossible to achieve [2]. Weight and aesthetics were important too. As a solution, much of the design process was focused on making the rotor as efficient as possible. Its four-rotor configuration and autonomy together increase the controllability and pilot safety.

After conducting an extensive configuration trade-off analysis, a quadcopter was deemed to be the best configuration for addressing the RFP (see Chapter 2). Key justifications for this choice are as follows. Four vectors of thrust provide greater stability than in a single rotor configuration. With the Aerial Screw rotors being taller than conventional helicopter rotors the quadcopter configuration will prevent the aircraft from being excessively tall. The pilot is positioned in the center of the quadcopter structure, keeping the center of gravity low, increasing the stability and subsequently increasing pilot safety.

3.1 Preliminary Vehicle Sizing

An in-house sizing code was developed using modified momentum theory to estimate the GTOW and power requirements of *Samara*. While this methodology is quite general in its applicability, the code modifies several standard equations and parameters to provide the flexibility to perform analysis for the mission specified in the RFP. Trade studies were conducted to examine the merits of varying the number of rotors, their dimensions, disk loading, tip speed, and classification of powertrain. Using the trade study results, a *Samara's* preliminary vehicle sizing was calculated.

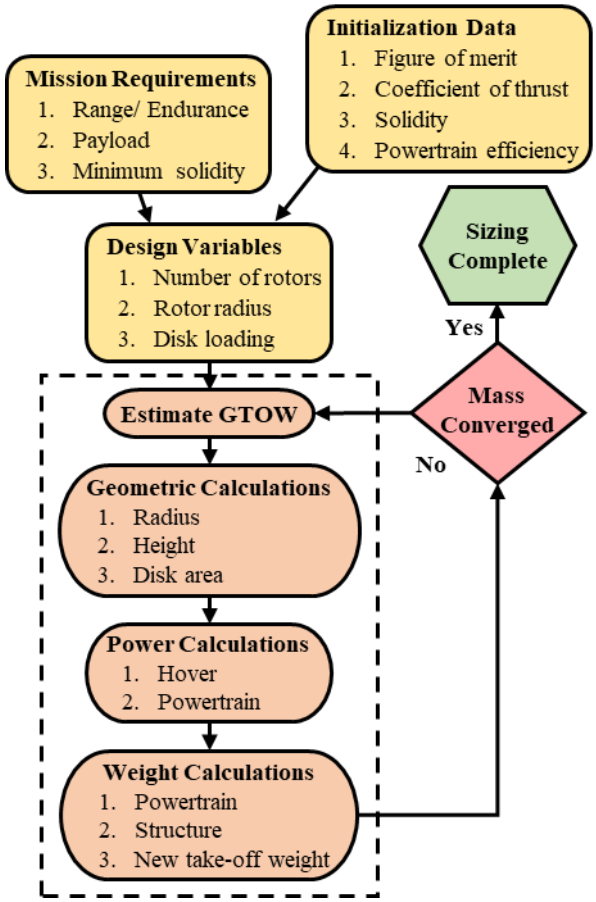

Figure 3.1: Flowchart for the vehicle sizing procedure

3.1.1 Description of Sizing Algorithm

The flowchart for the sizing methodology is depicted in Figure 3.1. The sizing code uses an iterative process that begins with the specification of inputs, which includes both mission-specific parameters such as range, endurance, payload, and minimum solidity, as well as vehicle-specific information, such as powertrain efficiencies, number of rotors, figure of merit, coefficient of thrust, disk loading, and rotor dimensions.

Ramasamy [8] shows the metrics used to extrapolate the model scale results to full scale. The relationship between power loading (PL), disk loading (DL), and Figure of Merit (FM) can be expressed as shown in Equation 3.1.

$$PL = \frac{\sqrt{2\rho}FM}{\sqrt{DL}} \qquad [3.1]$$

This concept is supported further by CFD simulations of the full-sized rotors (discussed in detail in Chapter 4).

3.1.2 Disk Loading Parametric Study

The final iteration of the sizing code consisted of a DL parametric study. This variable may be assigned any value since it has a direct relationship with the tip speed of the rotor. The formula to calculate the DL is derived in Equation 3.2.

$$DL = \frac{T}{A} = \frac{C_T \rho_0 A v_{tip}^2}{A} = C_T \rho_0 v_{tip}^2 \qquad [3.2]$$

The purpose of the parametric study was to find the DL corresponding to the minimum GTOW. To do this, the sizing algorithm was inserted into a loop. The data produced is illustrated in Figure 3.2 as the relationship between the GTOW and DL. The resulting DL is 10.8kg/m^2 (2.2lb/f t^2). Each data set is the summation of the weight of the one directly below, so the top set represents the GTOW of *Samara*. The black line intersects the other sets at the minimum GTOW.

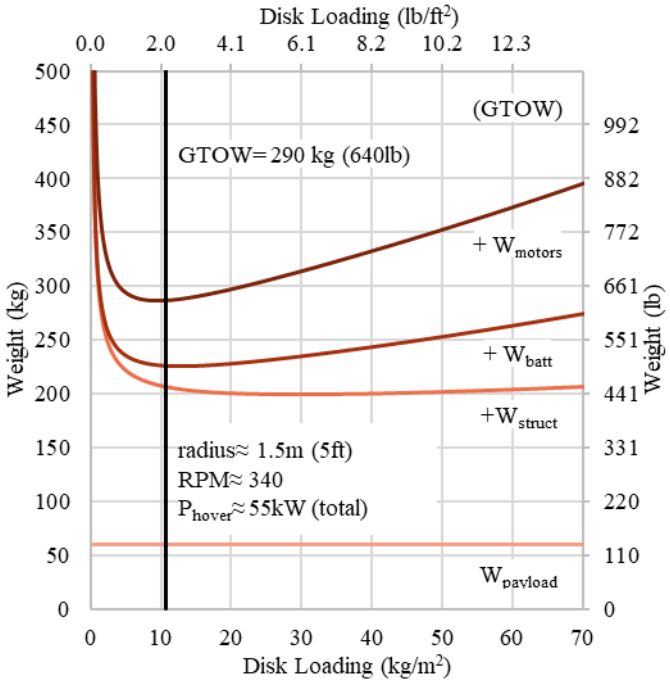

Figure 3.2: Disk loading parametric study

4 Concept Validation

Before designing *Samara*, it was crucial to develop an understanding of the aerodynamics of an Aerial Screw. No analytical model exists that describes the aerodynamics of this type of rotor. The best of course of action was to conduct small scale tests to characterize the performance of different configurations of Aerial Screws. This testing provided valuable metrics governing efficiency, performance, and sizing that helped guide the design process.

4.1 Evolution of Design

One of the main features that separates Aerial Screws from other traditional rotor designs is the Aerial Screw's high solidity. It is not well understood how such a high solidity effects air flow and rotor performance. The evolution of scale model rotor characteristics is listed in Table 4.1.

4.2 Testing Setup and Procedure

Tests were performed using 3D printed small-scale models. These prints were done in Polylactic Acid (PLA), which is typically the cheapest and most versatile filament. Using PLA allowed design iterations to be tested rapidly and inexpensively. Each rotor was evaluated using one of two test stands: a stand with embedded thrust and RPM sensors, supplemented with a multimeter for current measurements (TS1), and a stand with embedded thrust, RPM, torque, current, and voltage sensors that record at 30 Hz (TS2).

Table 4.1: Evolution of scale model rotor characteristics

Stage	Key Design	Goal	Outcome	Reference
1	Simple flat plate rotor blades.	Understand the impact of increasing simple rotors solidity of over multiple iterations.	High-solidity flat-plate rotors require increased pitch angles to produce acceptable levels of thrust.	Figure 4.6
2	Slotted high solidity flat plate rotor blades – influenced by research conducted on multi-element rotors.	Understand the impact on lift and power required, by introducing gaps throughout a high-solidity rotor.	Introducing gaps improved rotor performance. However, the slotted blade concept was ultimately abandoned after Leonardo Helicopters clarified rotor design requirements.	Figure 4.9
3	Single turn Aerial Screw	Analyze the performance of a rotor that resembled da Vinci's original design by modifying the number of rotations and pitch angle.	da Vinci's design produced adequate levels of performance but had inherent instability due to mass imbalance, causing enormous vibration.	Figure 4.13 Figure 4.14 Figure 4.17
4	Double Turn, Single Surface Concentric Aerial Screw.	Eliminate the instability exhibited by the continuous Aerial Screw model.	Aerodynamic and mass imbalances were successfully eliminated.	Figure 4.20
5	Half-Turn Aerial Screw.	Evaluate change in performance from an increase in the root pitch.	Performance gains come at the expense of increased rotor height, subsequently increasing vibrations.	Figure 4.21
6	Tapered single surface concentric Aerial Screw.	Minimize power required by eliminating low-pitch blade area that may not contribute to thrust production.	Produced the final design. It is scalable and provides the efficiency and performance needed to complete the mission outlined in the RFP.	Figure 4.28

Originally, the intention was to conduct preliminary tests on TS1 to allow rapid iteration, followed by verification on TS2. This procedure was followed until the University of Maryland closed access to TS2 in response to the COVID-19 pandemic. Fortunately, TS1 was mobile enough to allow it to be taken home by a team member, allowing testing to continue.

Test results from TS2 were used to supplement the results collected using TS1 (discussed in more detail in Chapter 4.3.2). Thus, the test results gathered from TS1 are comparable in quality

Figure 4.1: TS1

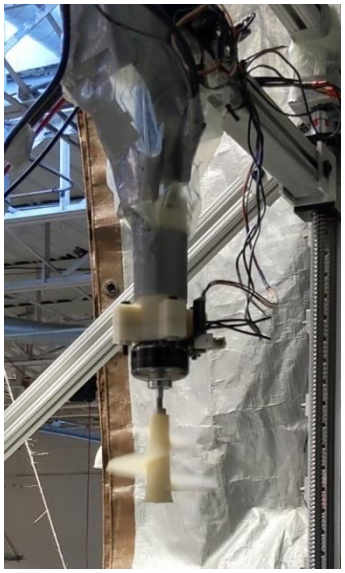

Figure 4.2: TS2

To analyze the efficiency and performance of the rotors, the following quantities were recorded:

- Thrust – generated by the rotor, measured by a load cell in grams
- RPM – rotational rate of the motor and rotor, measured by a Hall effect sensor (TS2) or calculated from the motor's Pole Pairs (TS1)
- Shaft Torque – measured by a torque cell (TS2) or extrapolated from power (TS1) (see Chapter Relating Electric and Mechanical Power)
- Power – calculated from the voltage and current drawn by the motor

The equations for the metrics used to quantify rotor performance are listed below:

$$Coefficient\ of\ Thrust: C_T = \frac{T}{\rho A V_{tip}^2} \quad [4.1]$$

$$Power\ Loading: PL = \frac{T}{P} = \frac{C_T}{V_{tip} C_P} \quad [4.2]$$

$$Coefficient\ of\ Power: C_P = \frac{P}{\rho A V_{tip}^3} \quad [4.3]$$

$$Disk\ Loading: DL = \frac{T}{A} \quad [3.2]$$

$$Figure\ of\ Merit: FM = \frac{C_T^{1.5}}{\sqrt{2} C_P} \quad [4.4]$$

$$Solidity: \sigma = \frac{N_b c}{\pi R} = \frac{\theta(a^2+ab+b^2)}{6\pi b^2} \quad [4.5]$$

The first equality within Equation 4.5 is the conventional definition of solidity (σ): the projected surface area of the blade (A_{tot}) divided by the rotor disk area (A_{disk}). However, this equality doesn't apply to Aerial Screws because the radius (r) varies throughout, the number of blades (N_b) is equal to one, and the best value for chord length (c) is the circumference of the disk area. The second equality was derived in house to make the equation applicable to single rotor Aerial Screws. The major change exhibited here is A_{disk} is defined as the area of the disk bounded by the outermost radius of a tapered screw with a= minimum radius, b= maximum radius, and θ= angle turned from leading edge to trailing edge

4.3 Test Equipment

A Gartt ML 4108 DC brushless motor (620Kv) was used on both test stands. Power was provided by a three cell, lithium-ion polymer battery through a 3A electronic speed controller. TS2 collected raw data from load and torque sensors using an Arduino micro controller and delivered the data in real time to a computer through a serial port at 30Hz.

TS1 has no similar data recording mechanism. To record test data using this stand, a video was made of the thrust stand's display screen to capture all relevant data. The information was later extracted from the video and documented for analysis.

4.3.1 Flow Visualization

Flow visualization was performed so the air flow could be studied visually and compared with the test results and influence succeeding rotor designs. Smoke was generated by a fog machine (see Figure 4.3).

The smoke was directed towards the rotors mounted to TS1. Efforts were made to ensure that the flow entering the rotor was undisturbed, and the quality of these visualizations improved with practice and time. Still images from these videos are shown throughout Chapter 4 to illustrate the flow patterns through the test rotors.

Figure 4.3: Fog machine used for flow visualization

4.3.2 Relating Electric and Mechanical Power

As mentioned previously, the experiments performed as part of this testing program took place on two different thrust stands. It is inevitable that any change in the testing equipment will affect the results and introduce error when comparing results between the two. Every effort was made to limit the number of variables that differed between TS2 and TS1. For example, the same motor (Gartt ML 4208) and power supply (3 cell LiPo) were used with both test stands. This minimized any changes to the efficiencies of the powertrain when moving from one system to the other.

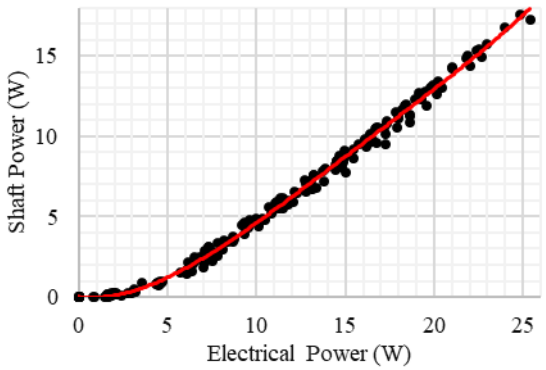

Figure 4.4: Relationship between shaft power and electrical power

The absence of an embedded torque cell within TS1 was a key hurdle when comparing the results between TS1 and TS2. This meant that motor torque could not be measured directly. This presented a significant problem since motor torque is used to calculate power required and subsequently calculating the coefficient of power and FM of the rotor. To overcome this problem, data was used from TS2 test results to find a relationship between electrical and mechanical power. This relationship is shown in the Figure 4.4 for all the test data collected on TS2. Power metrics were calculated using the torque (Q), RPM, battery voltage (V), and current (I) measured by TS2 (see Equation 4.6 and Equation 4.7).

$$P_{shaft} = Q * \Omega \text{ [W]} \quad [4.6]$$

$$P_{elec} = V_{bat} * I_{bat} \text{ [W]} \quad [4.7]$$

This data includes Aerial Screws, flat plate rotors, slotted rotors and more. A fourth order polynomial was fit to this data. The relationship appears linear above 7W, but the fourth order polynomial captured the relationship better for the low-power tests. The best-fit equation is shown in Equation 4.8.

$$P_{shaft} = 6 * 10^{-5} P_{elec}^4 - 0.0037 * P_{elec}^3 + 0.0897 * P_{elec}^2 - 0.1195 * P_{elec} + 0.0104 \quad [4.8]$$

As previously mentioned, the powertrain (including motor, ESC and battery) are the same for both test stands, this equation allows one to extract shaft power from electrical power, even for tests done on TS1 which is not able to directly measure motor torque.

4.4 Results

4.4.1 Stage 1: Initial Testing: FM = 0.05

The first tests conducted had two purposes: to calibrate and set up the test equipment and test procedures, and to analyze the effect of blade solidity and pitch angle on performance. The specifications of the rotors tested are listed in Figure 4.6. These initial tests were done on TS1.

The results of these tests show that performance levels decrease for flat-plate rotors as chord length increases, and performance increases as pitch angle increases. The effect of chord length can be seen when comparing the 2 rotors at 10-degree pitch angle: the Quarter Solidity rotor produced more thrust than the Half Solidity rotor. Similarly, the Half Solidity rotor with four blades performed better than the Half

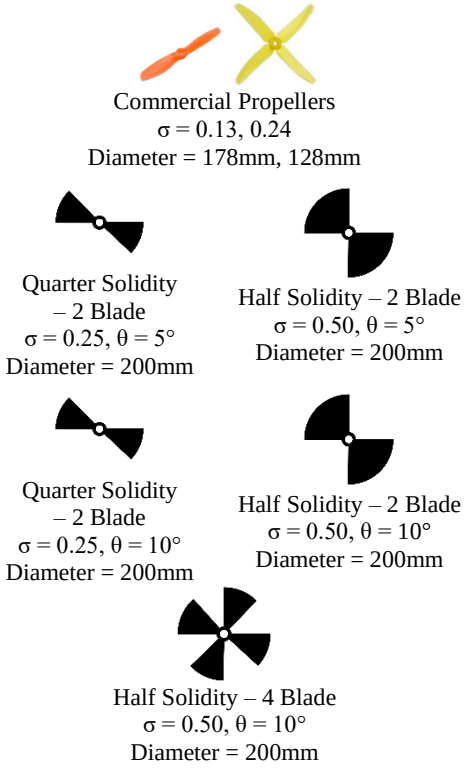

Figure 4.6: Rotor profiles for initial testing

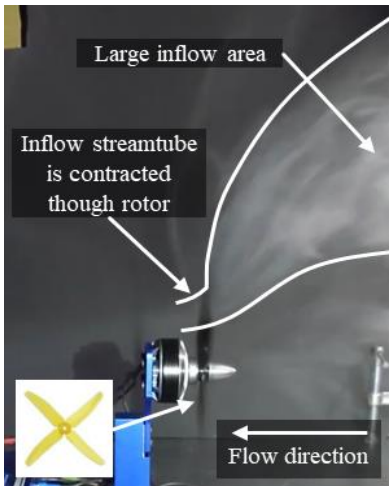

Figure 4.5: Flow visualization of σ = 0.24 commercial rotor

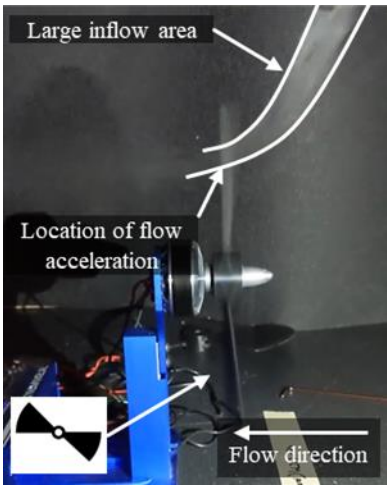

Figure 4.7: Flow visualization of σ = 0.25, θ = 10° rotor

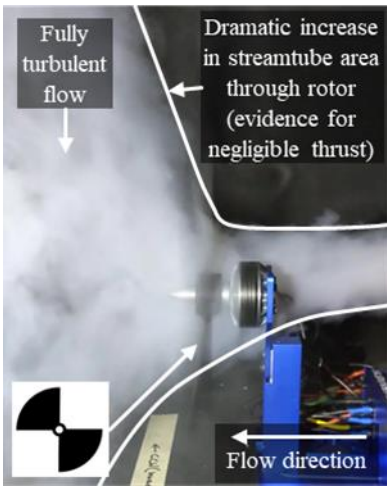

Figure 4.8: Flow visualization of σ = 0.25, θ = 10° rotor

Solidity rotor with only two blades. The effect of pitch angle is also apparent from these results. For the Quarter Solidity rotors, the rotor at the higher pitch angle performed better.

Flow visualizations from these initial tests are in shown in Figure 4.7, Figure 4.8, and Figure 4.5. It is apparent that the rotors that performed poorly in the tests also exhibit suboptimal flow patterns. As the flow passes through these rotors, it becomes turbulent and is redirected outward into a wide cone. This is the opposite of what is expected from an efficient rotor design. The downwash should be contracting and forming a clear stream tube as flow exits the rotor. Thus, the flow visualizations confirm and support the conclusions from testing.

4.4.2 Stage 2: Slotted Blades: FM = 0.05

The best performing rotors from the stage 1 were tested on TS2. Additionally, a new rotor concept was developed building on the conclusions drawn from Stage 1 test results and flow visualizations. As stated in Chapter 4.4.1, one of the main conclusions from the initial tests was that for a rotor with a given solidity, shorter chord lengths generally perform more efficiency than longer chord lengths. It follows that, subdividing each rotor further should result in improved performance, up to a limit. This motivated the design and testing of the slotted rotor shown in Figure 4.9.

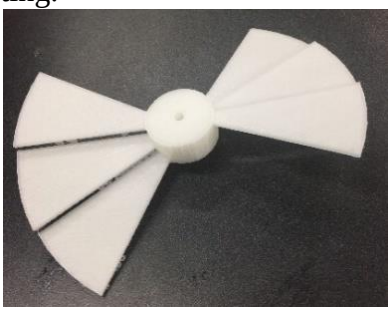

Figure 4.9: Slotted-half-solitity blade:
Diameter = 200 mm
$\theta_{root} = \theta_{tip} = 10°$
σ = 0.5

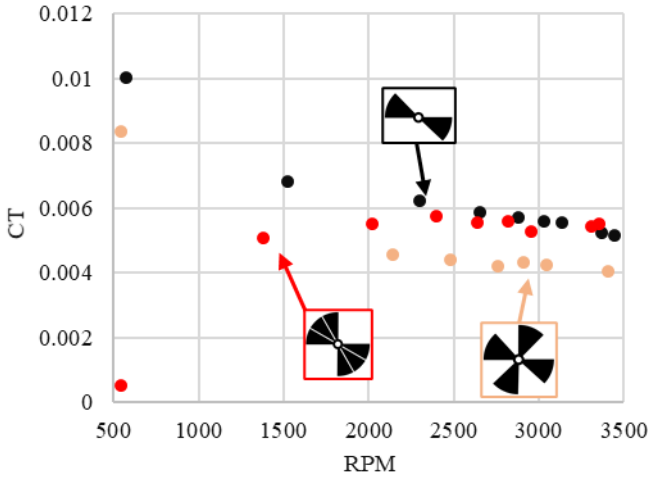

Figure 4.10: Coefficient of thrust vs. RPM of slotted rotor and well performing rotors from Stage 1

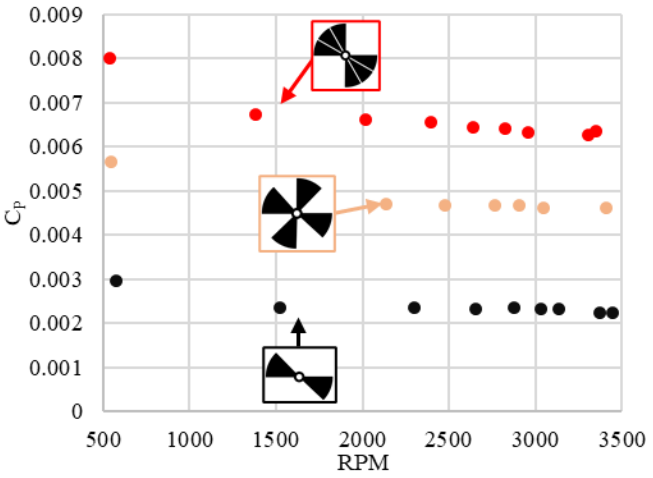

Figure 4.11: Coefficient of power vs. RPM of slotted rotor and well performing rotors from Stage 1

Test results for the slotted blade are compared with the top performing configurations from the initial tests – the two bladed Quarter Solidity and four bladed Half Solidity rotors – in Figure 4.10 and Figure 4.11.

Flow visualization for the slotted blade was also performed. The flow through a blade appears to be more aligned with what is expected from a traditional rotor – the flow contracts and accelerates as it passes through the blade, and the downwash is directed axially. The added slots, then, clearly improve performance when compared to the Half Solidity rotor with two blades.

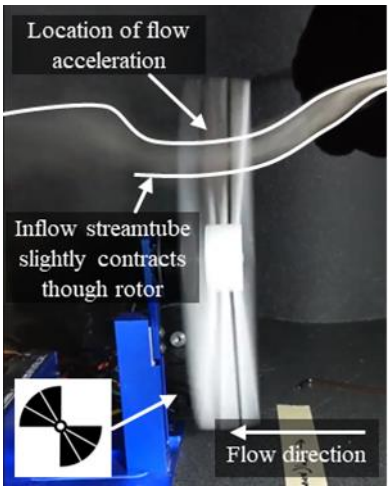

Figure 4.12: Flow visualization of $\sigma = 0.25$, $\theta_{root} = \theta_{tip} = 10°$ rotor

4.4.3 Stage 3: Single Turn Aerial Screws

From the data obtained in stage 2, two new 3D printed rotors were produced: a single-turn Aerial Screw, and a single-turn Aerial Screw with slots.

When these rotors were tested on TS2 a problem with the design became apparent. Vibrations began at approximately 1000 RPM and their amplitude increased with RPM. The persistent and severe vibrations produced inconsistent torque and thrust readings from both rotors.

Flow visualization was obtained by limiting the rotor RPM to below its resonant frequency (see Figure 4.19). The flow visualization shows promise that the screw would perform well if the vibration issues could be solved. This further motivated the design to solve the vibration issue.

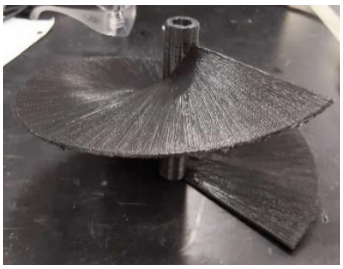

Figure 4.13: Single-turn Aerial Screw
Height = 100 mm
Diameter = 200 mm
$\theta_{root} = 58°$, $\theta_{tip} = 9°$
$\sigma = 1$

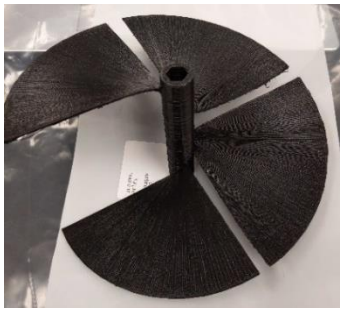

Figure 4.14: Single-turn Aerial Screw with slots
Height = 100 mm
Diameter = 200 mm
$\theta_{root} = 58°$, $\theta_{tip} = 9°$
$\sigma = 2$

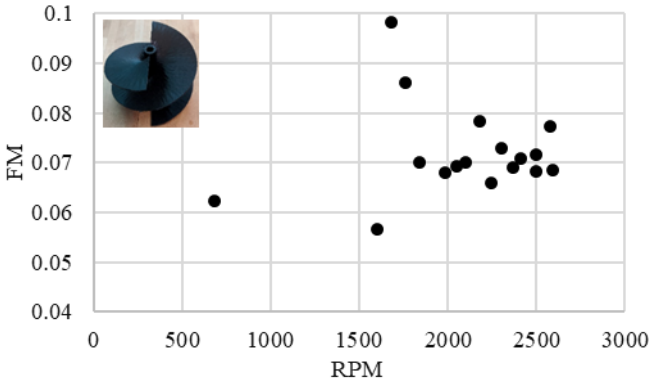

Figure 4.15: FM vs. RPM of a Double-Turn, Single Surface, Concentric Aerial Screw

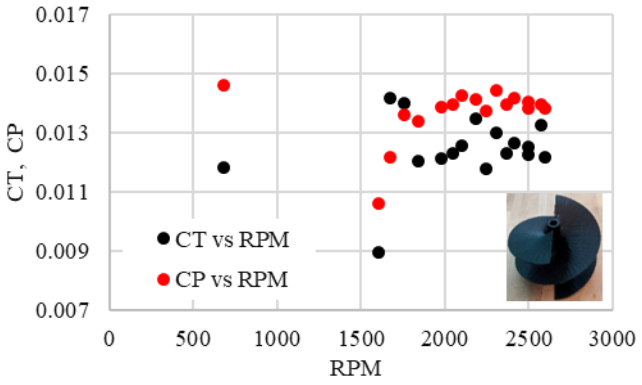

Figure 4.16: C_T and C_P vs. RPM of Double-Turn, Single Surface, Concentric Aerial Screw

Despite the inability to generate results for a full-turn Aerial Screw over the full testing RPM spectrum, the discovery of this rotor's resonance did reveal a major design flaw in da Vinci's concept. When an Aerial Screw is supported at only one end (see Figure 4.17), there is an imbalance when the screw rotates, even if the center of mass is perfectly aligned with the axis of rotation. The distribution of mass along the surface of the screw creates a centrifugal force on the blade when rotated. This produces an unbalanced moment about the motor which causes the violent vibrations observed during testing (see Figure 4.17).

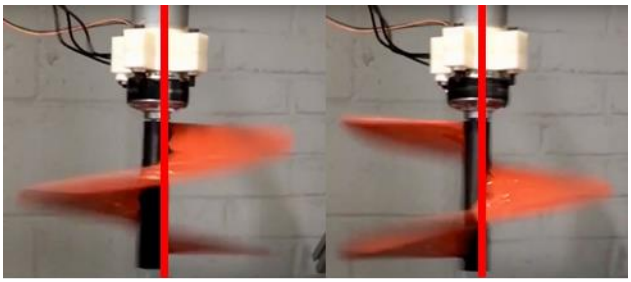

Figure 4.17: Still images from a video showing inherent vibrations of a Single-Turn Aerial Screw

Similarly, the geometry of the Aerial Screw suggests that there may be another source of a vibration-producing moment: the lift force. Assuming the center of lift acts somewhere between the leading and trailing edges, and somewhere between the blade root and tip, the center of lift does not act along the axis of rotation of the Aerial Screw. (see Figure 4.17). For a single turn screw with a solidity of one, it would be nearly impossible to align the center of lift and the axis of rotation of an Aerial Screw. This would add to the vibrations produced by the mass imbalance and could be catastrophic for an Aerial Screw powering a full-sized vehicle.

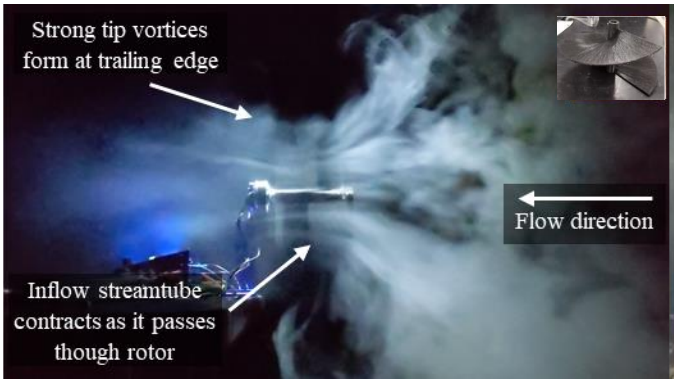

Figure 4.18: Flow visualization of Single-Turn Aerial Screw

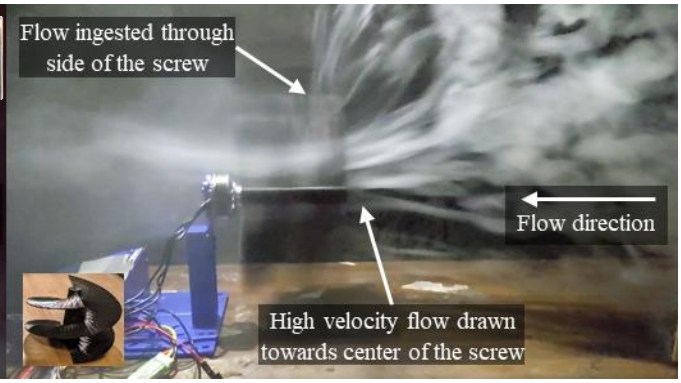

Figure 4.19: Flow visualization Double-Turn, Single Surface, Concentric Aerial Screw

4.4.4 Stage 4: Double-Turn, Single Surface, Concentric Aerial Screw Tests: FM = 0.075

To account for this aerodynamic and geometric imbalance, a Double-Turn, Single Concentric Aerial Screw was designed (see Figure 4.20). This design solves both imbalances simultaneously. Tests were performed to confirm this and to evaluate the performance of Double-Turn, Single Surface, Concentric Aerial Screw.

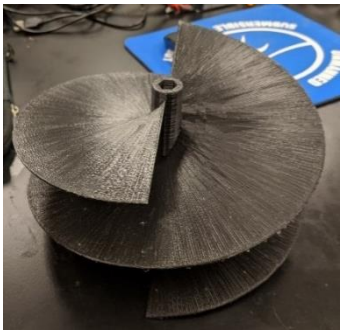

Figure 4.20: Double-Turn, Single Surface, Concentric Aerial Screw

The results of these tests showed the best performance achieved up to this point (see Figure 4.15 and Figure 4.16). Additionally, vibrations were greatly reduced, suggesting that the Single Surface, Concentric Aerial Screw the mass and aerodynamic imbalances observed in the Single-Turn Aerial. Flow visualization confirms that this design draws flow into the rotor, contracts the stream tube, and accelerates the flow axially, producing thrust (see Figure 4.19).

4.4.5 Stage 5: Half-Turn Aerial Screws (effect of root pitch angle): FM = 0.45 (H=75mm), FM = 0.04 (H = 50mm) (2500 RPM)

Initial testing showed that increasing root pitch angle increases the performance of high-solidity rotors, and taller rotors are more susceptible to vibrations. There is an inherent trade-off between root pitch angle and rotor height. The height (h) is related to the root pitch angle for a given hub diameter as follows:

$$h = \pi * d_{hub} * \tan\theta_{root} \quad [4.9]$$

Two Half-Turn Aerial Screws were printed to examine this relationship (see Figure 4.21). This allowed the pitch angle and height to be increased while minimizing the impact of vibrations. The results of these tests, including flow visualizations, are shown in Figure 4.19.

Increasing the root pitch (and the height) produces more thrust, but it also requires more power. Overall efficiency was better for the higher-pitch rotor, but the slight increase in performance must be considered against the potential for amplified vibrations. The test results suggest that the smaller pitch angle of the two would be more appropriate for a full-turn, double Aerial Screw.

Diameter = 150mm	Diameter = 150mm	Diameter = 150mm
σ = 1	σ = 1	σ = 2
Height = 50mm	Height = 75mm	Height = 100mm
θ_{root} = 57.8°	θ_{root} = 67.3°	θ_{root} = 57.8°
θ_{tip} = 12.0°	θ_{tip} = 17.7°	θ_{tip} = 12.0°

Figure 4.21: (From left to right) 2 Half-Turn Aerial Screws and a Double-Turn, Single Surface, Concentric Aerial Screw

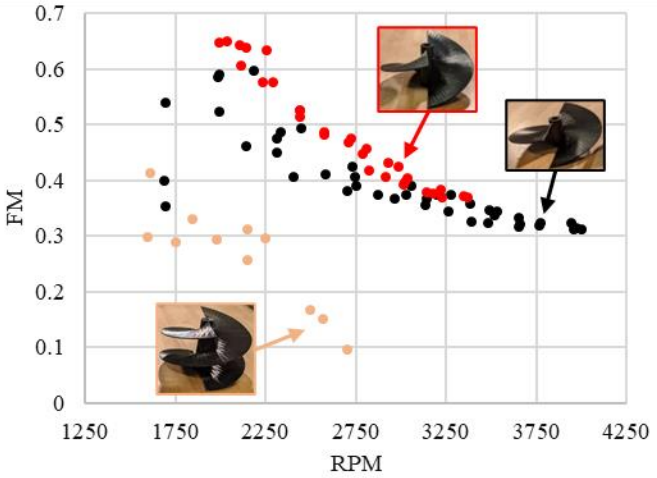

Figure 4.22: FM vs. RPM of Half-Turn Aerial Screws and Double-Turn, Single Surface, Concentric Aerial Screw

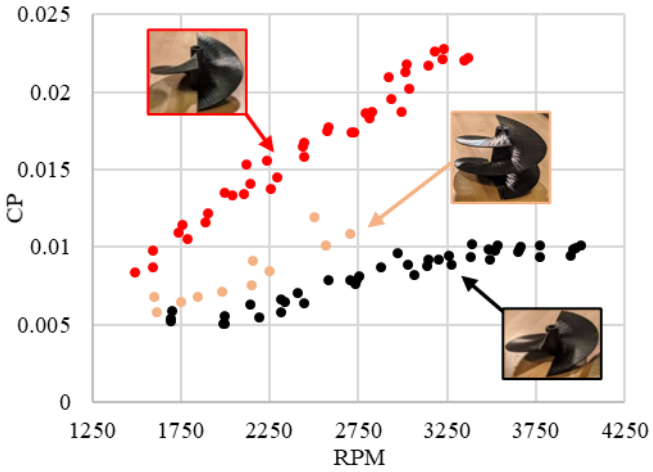

Figure 4.24: C_P vs. RPM of half-turn Aerial Screws and Double-Turn, Single Surface, Concentric Aerial Screw

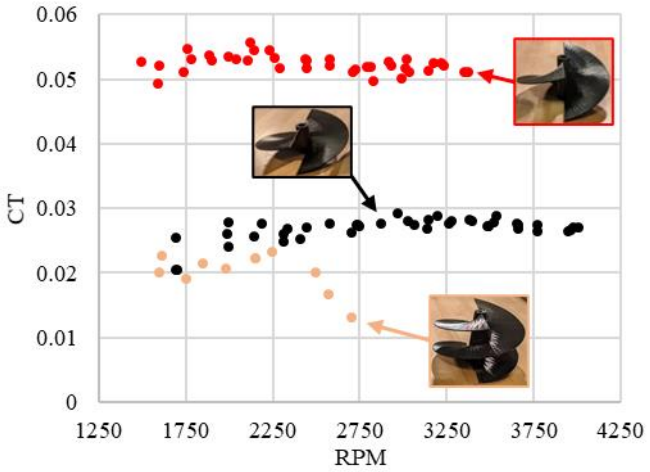

Figure 4.27: C_T vs. RPM of half-turn Aerial Screws and Double-Turn, Single Surface, Concentric Aerial Screw

A Full-Turn, Single Surface, Concentric Aerial Screw was printed with the same dimensions as the Half-Turn Aerial Screw (see Figure 4.21). This rotor was tested and showed slightly lower efficiency than the half-turn model.

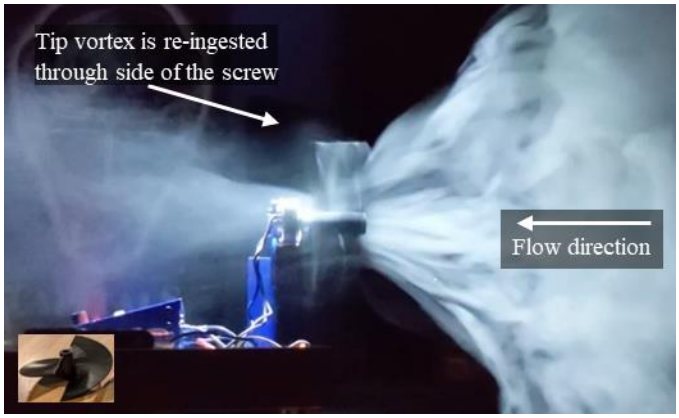

Figure 4.25: Flow visualization for half-turn Aerial Screw with 50 mm height, θ_{root} = 57.8°

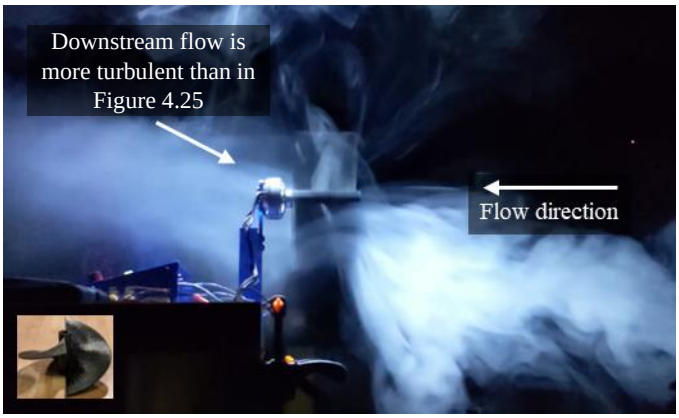

Figure 4.23: Flow visualization for half-turn Aerial Screw with 75 mm height, θroot = 67.3°

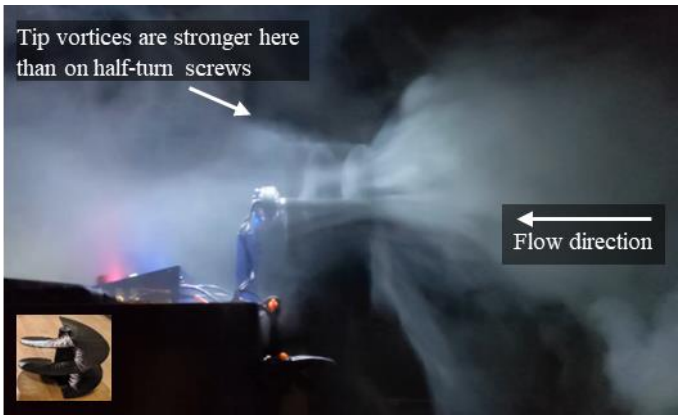

Figure 4.26: Flow Visualization for Double-Turn, Single Surface, Concentric Aerial Screw Aerial Screw, θ_{root} = 57.8°

4.4.6 Stage 6: Tapered, Single Surface, Concentric Aerial Screw: FM = 0.38

The final configuration tested was the Tapered, Single Surface, Concentric Aerial Screw (see Figure 4.28). This design closely matches da Vinci's original design, which also featured a screw with a radius that increases from top to bottom. Additionally, the taper removes some of the low-pitch blade surface from the outer edge of the screw, which could reduce drag losses and increase efficiency.

The test results and flow visualization for the tapered configuration are shown below. The taper was tested in both 'directions' (i.e. with radius increasing towards the top, and then towards the bottom (see Figure 4.28). Results confirm that da Vinci's orientation – smaller radius at the top, increasing in the direction of flow – produces the best performance. It is unclear what da Vinci's thought process was which led him to this configuration, but these results provide experimental evidence of the effectiveness of his design.

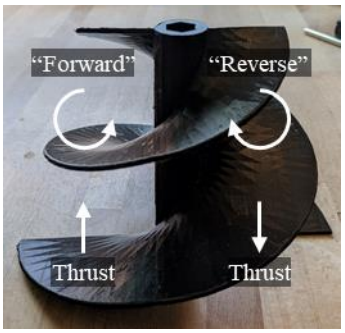

Figure 4.28: Tapered, Single Surface, Concentric Aerial Screw
Height = 100 mm, σ = 1.21
Diameter = 78 mm (top), 150 mm (bottom)
θ_{root} = 57.8°, θ_{tip} = 22° (top), 12.0° (bottom)

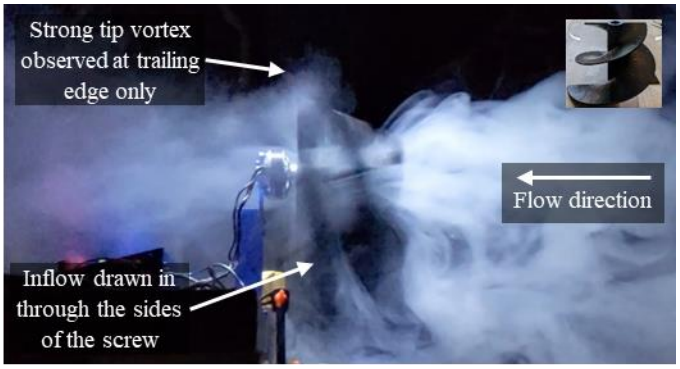

Figure 4.29: Flow visualization of Tapered, Single Surface, Concentric Aerial Screw

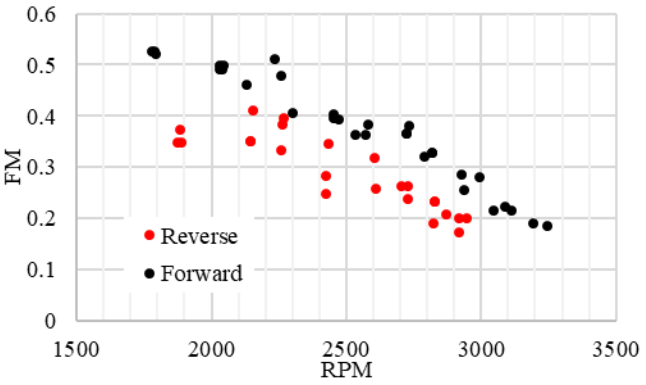

Figure 4.30: FM as a function of RPM of Tapered, Single Surface, Concentric Aerial Screw rotating "forwards" and "backwards"

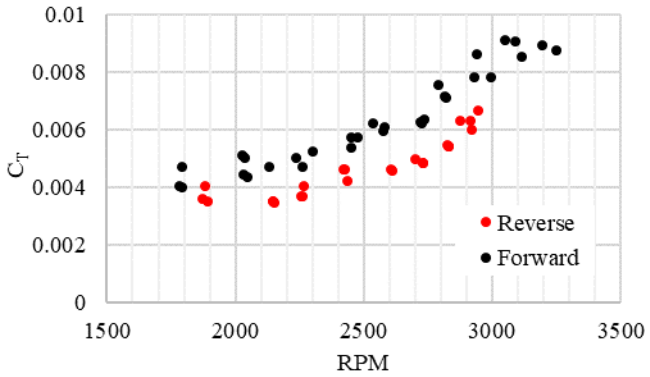

Figure 4.31: C_T vs. RPM of Tapered, Single Surface, Concentric Aerial Screw rotating "fowards" and "backwards"

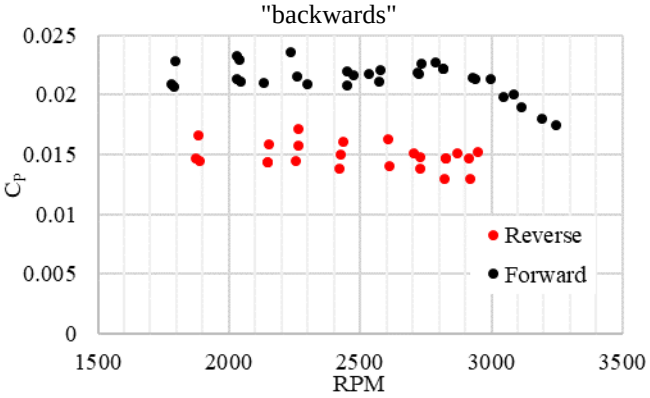

Figure 4.32: C_P vs. RPM of Tapered, Single Surface, Concentric Aerial Screw rotating "fowards" and "backwards"

4.5 2D CFD

The first set of CFD calculations were performed to create an optimal design for a slotted blade rotor (see Chapter 4.4.2). To optimize this design, CFD was performed to determine the ideal vertical distance and increasing pitch between each segment. The conclusions were a gap of 0.15 chord and 0.75 radius from the center and a downturn angle of 5 degrees between segments. No horizontal gap was evaluated due to the RFP solidity requirements.

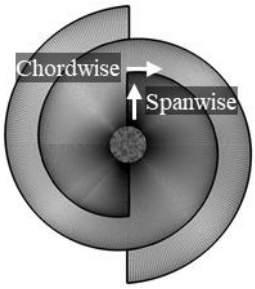

Figure 4.33: Top down view of surface mesh

4.6 3D CFD

The second set of CFD simulations performed were conducted later in the design process. These utilized a method designed by University of Maryland personnel to simulate aerodynamic flows using Hamiltonian loops and strands grids [9]. This approach applies three-dimensional unsteady Reynolds-Averaged Navier-Stokes equations that are solved on overset grids [9]. The simulations employs a fifth-order WENO scheme, second-order dual-time stepping, a Medida-Baeder transition model and a hybrid Spalart-Allmaras-Delayed Detached Eddy Simulation turbulence model [9]

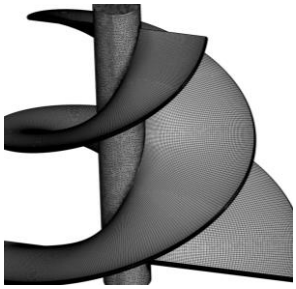

Figure 4.34: Isometric view of surface mesh

The surface mesh on the rotor was split into two sections. Along the blade surface, a structured mesh was used. This structured mesh uses 95 points along the spanwise direction and 330 points in the chordwise direction, as defined in Figure 4.33. This results in a total of 127,232 quadrilateral elements in the structured mesh. The rotor hub uses an unstructured mesh with 44,442 quadrilateral elements. Which is a total of 171,674 quadrilateral elements for the surface mesh.

Moving away from the surface of the rotor, approximately 60 strand layers are generated by extruding the surface (illustrated in red in Figure 4.35 and Figure 4.36). Further off the surface, there is a nested off-body background mesh (illustrated in blue in Figure 4.35 and Figure 4.37) which has a uniform grid spacing, but is more tightly woven than the background mesh that extends far beyond the surface (illustrated in green in Figure 4.35 and Figure 4.36).

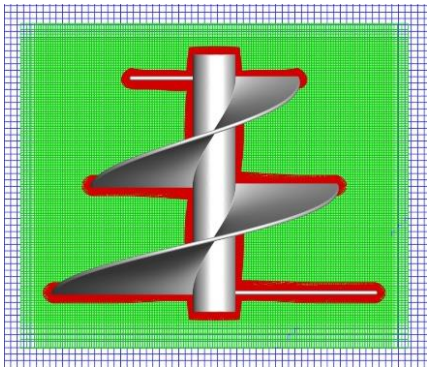

Figure 4.35: Full model view with strand layers (in red), nested off body background mesh (in blue), and uniform grid spacing (in green)

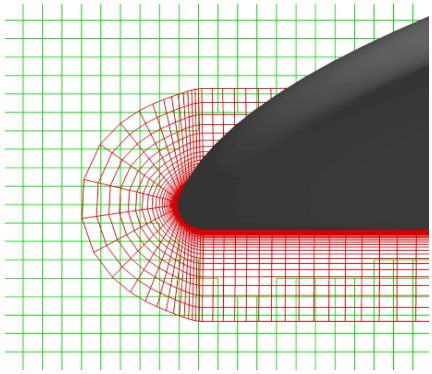

Figure 4.36: Close up view of rotor tip and surrounging strand layers (in red), and nested off body background mesh (in green)

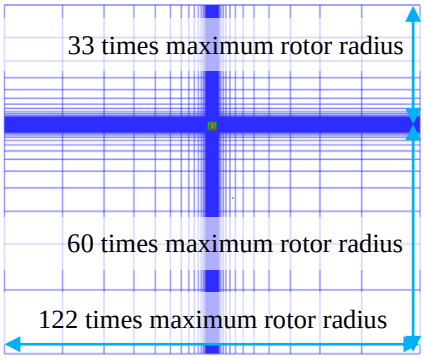

Figure 4.37: Uniform grid spacing (in blue) around model in center of figure

Using this modeling technique, two cases were performed, the first case, utilizing the same geometry as the scale model that was tested and chosen as the final design (see Figure 4.28), as well as a case utilizing that geometry scaled up to the dimensions produced by the sizing code (see Figure 3.2). The first case served to confirm the results that testing had provided, and the second case served to provide parameters about the final design, such as C_T and FM.

The first case utilized the design described in Chapter 4.4.6. Since the tests performed ranged in rotation speed from ~1700 RPM to ~3300 RPM, the average value of 2500 RPM was chosen to perform the CFD calculations. The results shown in Chapter 4.4.6 agree with the values obtained from testing.

The FM calculated from experimental testing at 2500 RPM was roughly 0.38. The value found through CFD was 0.35. Using standard values of density and speed of sound, the resulting C_T leads to a thrust of 0.2888N (0.0649lb). This is a lifting force capable of carrying 29 grams (0.0649lb). The thrust found experimentally was able to lift a mass of roughly 20 grams (0.044lb). The combination of these results shows that there is an agreement between the two procedures. Since these procedures agree, scaling the rotor size up to the size described by the sizing code and performing CFD will produce accurate results.

Table 4.2 : CFD results for R_{max} = 0.075m (2.95in)

RPM	2,500
Tip Mach Number	0.0574
Tip Reynolds Number	9,832
C_T	0.0346
C_P	0.013
FM	0.35

Table 4.3: CFD results for R_{max} = 1.518m (3.28ft)

RPM	340
Tip Mach Number	0.158
Tip Reynolds Number	5.47∃5
C_T	0.0365
C_P	0.0107
FM	0.46

4.6.1 Flow Visualization

Through performing CFD, some insight about how the rotor creates lift can be gained. The streamlines shown from the side (Figure 4.38) show that a significant portion of the inflow happens around the sides of the rotor. Thich is something that is supported by the flow visualization performed by the smoke generator. As shown in Figure 4.39, an interesting phenomenon occurred surrounding the tip vortex that started at the top of the rotor. This vortex separated from the normal tip vortex that stays at the tip of the blade. As shown in Figure 4.40, they interact with each other, but are largely separated. This phenomenon (coined the DaVi vortex) is the cause of a significant amount of thrust produced by the rotor

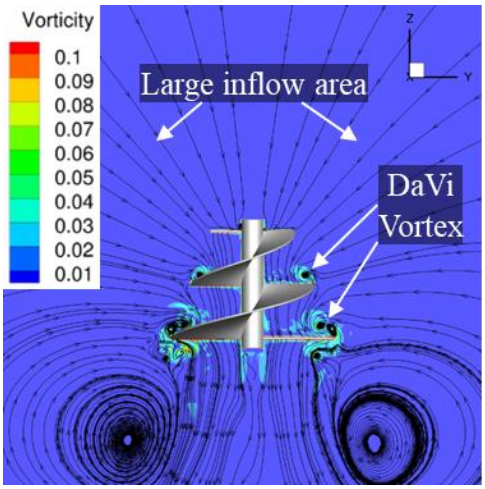

Figure 4.38: Streamlines of the rotor from the side

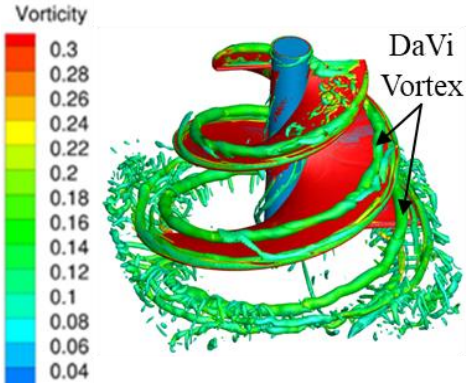

Figure 4.39: Visualization of vorticies on the final design

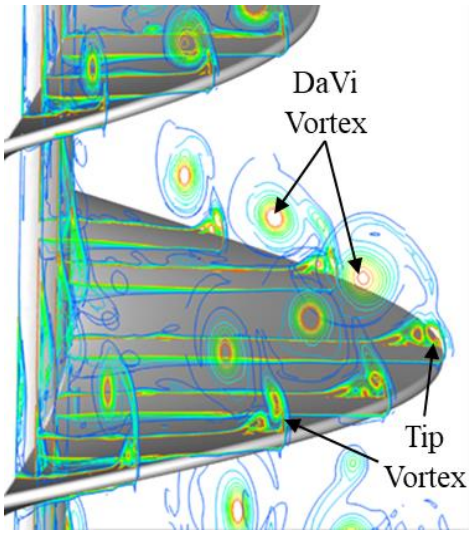

Figure 4.40: Interaction between tip vortex and DaVi vortex

5 Aerodynamics

5.1 Modeling High Solidity Rotors

With respect to da Vinci's original rotor design, widely used theories, such as Blade Element Momentum Theory, are not applicable when calculating the performance of an Aerial Screw due to several assumptions they make. Therefore, to gain essential metrics about the design, Scale model testing and CFD were used to generate data on the aerodynamics of the Aerial Screw. These methods ensured the generation of high-fidelity data.

5.1.1 Scale Model Testing

To overcome the lack of existing knowledge on Aerial Screw aerodynamics, a testing program was conducted to establish the basic aerodynamic principles and performance metrics associated with an Aerial Screw (see Chapter 4). Due to practical size limitations, testing was limited to small scale rotors, which necessitated scaling and verification to allow small-scale results to be translated to full-size vehicles.

Figure 5.1: 3D printed rotors used in scale model testing

Testing was carried out using 3D printed Aerial Screws. This allowed precise control over the design and modification of test rotors and allowing many design iterations to be tested.

Figure 5.2: Flow visualization performed for many test cases

Additionally, flow visualizations were produced using a smoke generator. These visualizations provided real-time insight into the air flow in and around the Aerial Screw. This flow visualization in combination with the thorough testing procedure created a more complete picture of the aerodynamics of Aerial Screws.

The conclusions drawn from test results became direct drivers of the final vehicle configuration and design specifications. More details about the test procedure, including results and flow visualization images, are provided in Chapter 4 of this report.

5.1.2 CFD

CFD was used in the design process to optimize design choices and validate scale model tests. Both 2D and 3D CFD were used during different stages of the design process (see Chapter 4.5 and Chapter 4.6).

2D CFD was used to optimize the parameters of a preliminary design. This adhered to the rotor solidity greater than one constraint but contained slits at several points along the surface of the blade. This concept was investigated when the results from testing a traditional da Vinci Aerial Screw yielded poor results.

Conducting this CFD yielded a FM of 0.46 (see Chapter 4.6). This is much larger than the value the sizing code provided. However, due to the complexity of performing 3D CFD analysis, this FM was discovered after the design was finalized using a lower value for FM. This insight shows that the design chosen is a conservative estimate, therefore allowing better performance than previously thought. Using the C_T found by the CFD results, the combination of all four rotors could support a GTOW of 385.4kg (849.6lb), which is much larger than the *Samara's* GTOW of 290kg (639.3). This allows for increased payload, and/or endurance.

6 Structure Geometry, Materials, and Aesthetics

Designing *Samara's* rotor to be a Tapered, Single Surface, Concentric Aerial Screw allows for a lighter airframe and better aerodynamic vehicle. A conventional Aerial Screw causes high instability and vibration because of the Aerial Screw's mass and aerodynamic imbalance (see Chapter 4.4.3). The moments produced by these imbalances are inherently eliminated with the Tapered, Single Surface, Concentric Aerial Screw

As noted in Chapter 2.1 one of the main design drivers was weight. To minimize the structure's contribution to *Samara's* GTOW, the lightest materials were selected. Optimizing the great specific strength of these materials, the Octatruss was designed (based off the Isotruss [7]). All dimensions are listed in Table 6.1 and Table 6.2. Additionally, *Samara* was designed to be assembled on site.

6.1 Rotor

Samara's rotor structure (see Figure 6.1) is composed carbon fiber tubing, aluminum 6061, Dacron, and fixtures such as epoxy, and bolts. This structure may be categorized into three sections: the central shaft, spars, helix, and fixtures. The shaft is at the center and spans the height of the rotor. Perpendicular to the central shaft are carbon fiber spars. These spars are bolted to the central shaft by aluminum spar mounting brackets. This

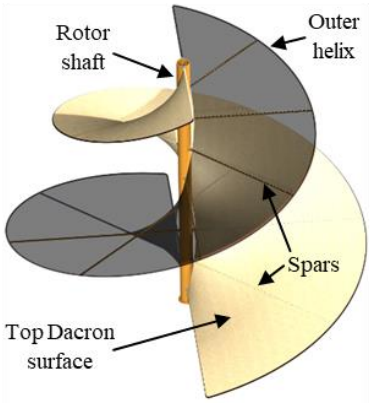

Figure 6.1: Rotor with transparent surface

bracket is connected to the central shaft with four bolts that pass through both the central shaft and both brackets; this allows for ease of assembly of the rotor.

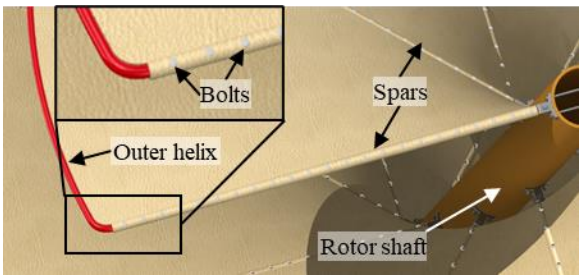

Figure 6.2: Top down view of rotor and some of its components

The lifting surfaces of the rotor are made with Dacron fabric. Dacron has a high strength to weight ratio and versatility. The rotor has a top and bottom layer of Dacron fabric. There are nine carbon fiber spars per helix that support the Dacron. Each successive spar is shorter than the last to create the rotor's taper. The carbon fiber spars are wrapped and epoxied to the outer carbon fiber helix with unidirectional carbon fiber. The Dacron fabric is bolted to the carbon fiber spars. These bolts may be removed for ease of deconstruction and on-site repairs.

6.1.1 Rotor Structural Analysis

Samara's carbon fiber spars are sized to withstand 1.4% of the GTOW (4.06kg (8.95lb)). One rotor contains 18 spars. In ANSYS, a parametric study was conducted to determine the best diameter and thickness for a hollow, cylindrical, carbon fiber spar with a tip deflection less than 5% of the total span. CFD showed the bottom 1.52m (5ft) spar supporting the largest lift forces so it was the basis for the sizing. Using carbon fiber rods with a longitudinal Young's Modulus of 120GPa (1.89Ǝ7psi) and a longitudinal tensile strength of 1500MPa (2.18Ǝ5psi), ANSYS calculated that the spars should be 0.25cm (0.1in) thick with an outer diameter of 2.54cm (1in). This yielded a safety factor of 22 and a tip deflection of 2% of the total span (see Figure 6.3 and Figure 6.4).

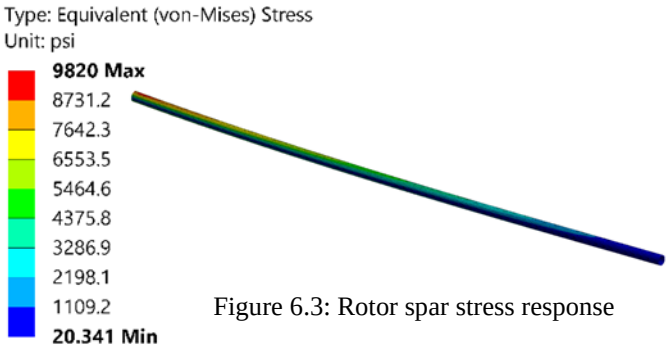

Figure 6.3: Rotor spar stress response

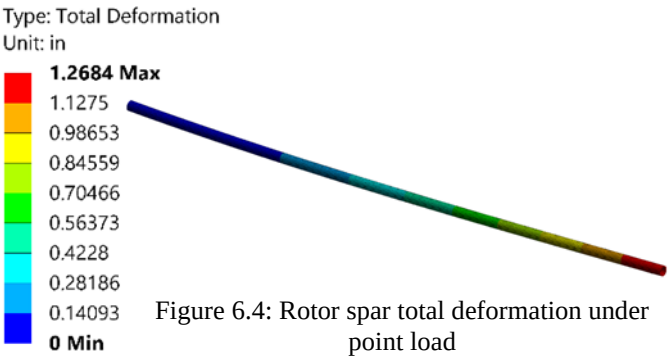

Figure 6.4: Rotor spar total deformation under point load

6.2 Landing Gear

At the base of each landing gear is a Sorbothane half sphere and 5 damping cylinders. These are shock absorbers to ensure pilot safety and vehicle longevity. These shock absorbers screw and epoxy into Samara's aluminum powertrain enclosure. Aluminum 6061-T6 was chosen for the powertrain enclosure due to its high strength and energy absorption capabilities – in the event of a hard landing. The enclosure includes vents for air-cooling to mitigate overheating.

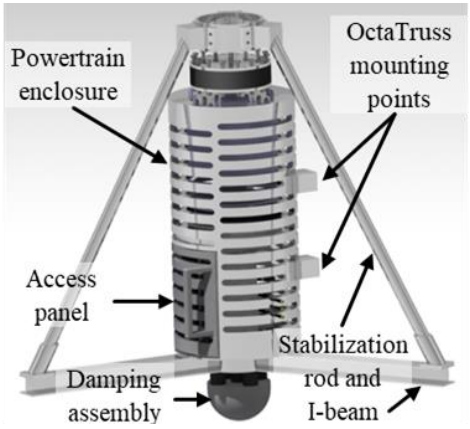

Figure 6.5: Landing gear assembly

Mounted perpendicularly beneath the powertrain enclosure are 3 I-beams accompanied with their own stabilizing rods. These rods dampen moments developed within the rotor. The stabilizing rods are joined at their apex with a bearing collar surrounding the rotor's shaft.

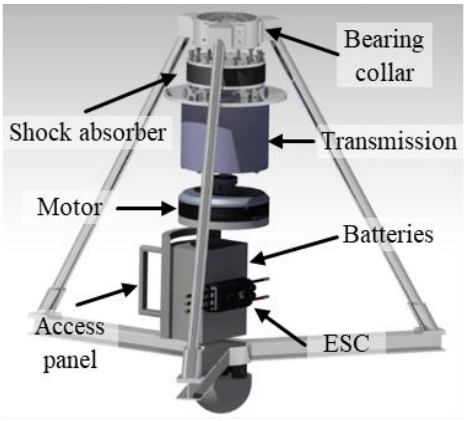

Figure 6.6: Landing gear without powertrain enclosure

From bottom to top, the powertrain enclosure holds two batteries, one electronic speed controller (ESC), one motor, and a transmission. The batteries are located at the bottom of the casing to provide separation from the electric motor to prevent overheating. A small panel allows the battery to be accessible for charging or replacement purposes. Above the battery is a metal plate mounted to the enclosure. This serves as a fixture for the electric motor. Shock absorbers are mounted below the motor and above the transmission for vibrational dampening. The OctaTruss arm is connected to the powertrain enclosure, opposite of the battery access panel.

6.2.1 Landing Gear Structural Analysis

Sorbothane is a proprietary, visco-elastic polymer. "As Sorbothane deforms the molecular friction generates heat. Energy is translated perpendicularly away from the axis of incidence causing the effect of the force to be pushed 90° out of phase from original disturbance" [10]. The high damping coefficient reduces the impact force up to 80% as displayed in Figure 6.7: Sorbothane impulse response. Sorbothane also has low transmissibility at resonance as displayed in Figure 6.8: Sorbothane transmissibility at resonance. Its ability to absorb shock is guaranteed for millions of cycles [11].

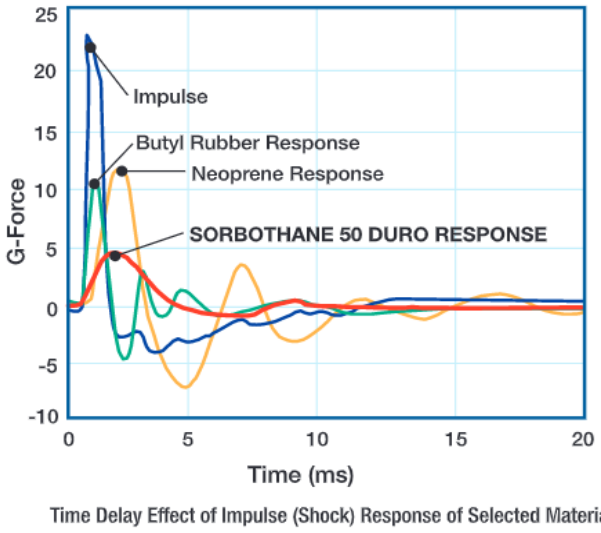

Figure 6.7: Sorbothane impulse response

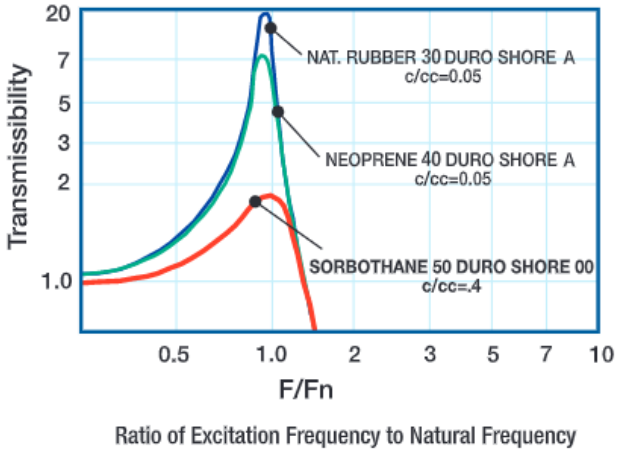

Figure 6.8: Sorbothane transmissibility at resonance

The half sphere and cylindrical shock absorbers use a 70-durability shore 00 for a dynamic Young's Modulus at 15 hertz. The tensile strength at break is 1.32MPa (191psi). By conducting Finite Element Analysis (FEA), Figure 6.9 and Figure 6.10 were rendered: they illustrate *Samara's* landing gear's stress response and total deformation when the vehicle lands at a 45-degree angle with respect to the ground. The magnitude of the vector is one-fourth of

the GTOW – 72.6kg (160lb). The max equivalent stress that occurs is 105 kPa (15.25 psi); therefore, this design has a safety factor of 12.52.

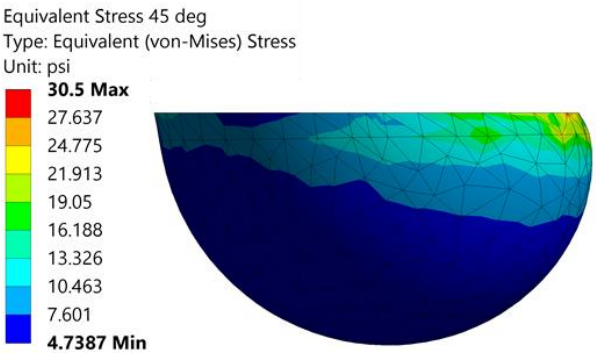

Figure 6.9: Sorbothane landing gear shock absorber stress response

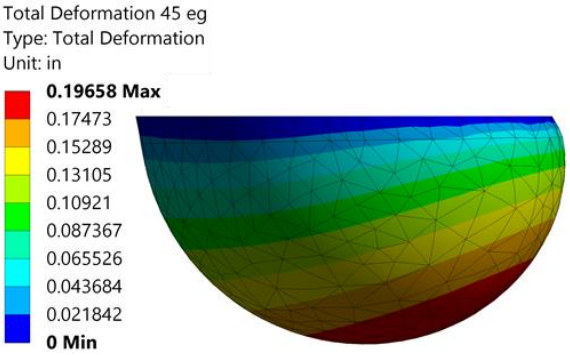

Figure 6.10: Sorbothane landing gear shock absorber deformation response

The three stabilization I-beams are made of Aluminum 6061-T6 with a tensile strength of 276MPa (4.5∃4psi) and a Young's Modulus of 68.9GPa (1∃3psi). Figure 6.11 and Figure 6.12 illustrate the max stress and deformation. Both are nearly negligible and therefore the structure has a large safety factor.

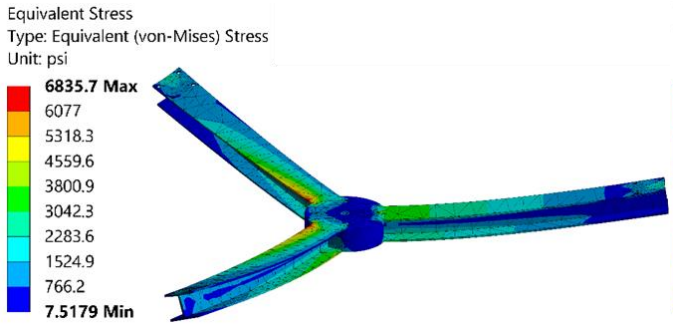

Figure 6.11: Stabilization I-beam stress response

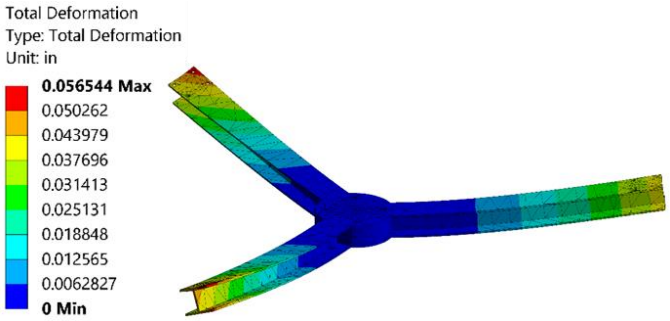

Figure 6.12: Stabilization I-beam deformation under multiple point loads

6.3 OctaTruss Airframe Structure

Samara's OctaTruss is the assembly of composite unidirectional carbon fiber and carbon fiber tubes with an octagonal cross-section. Each individual member carries primarily axial loads, taking full advantage of the inherent strength and stiffness of continuous fiber-reinforced composites.

Each diagonal member of the OctaTruss forms a 45-degree angled "X" along the circumference of the truss (see Figure 6.15). The longitudinal and diagonal members of the OctaTruss are epoxy coated carbon fiber rods. These rods have a longitudinal Young's Modulus of 120GPa (1.89∃7psi). The longitudinal tensile strength is 1500MPa (2.18∃5psi).

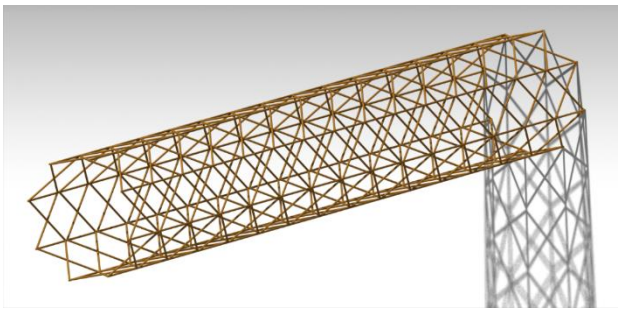

Figure 6.13: OctaTruss

Both sides of the OctaTruss are wrapped with epoxy coated carbon fiber sheets to prevent buckling at loading points. This carbon fiber composite sheet has a longitudinal Young's Modulus of 70GPa (1.02∃7psi) and a longitudinal tensile strength of 600MPa (8.7∃4psi). These wrapped ends of the OctaTruss are

epoxied inside aluminum caps. The aluminum end caps contain mounting holes for attaching the arm to the cockpit and landing gear assembly (see Figure 6.6 and Figure 6.19). The bolts feed through these holes and mate with nuts welded to the cockpit and landing gear assembly. There are 4 OctaTruss arms in the airframe.

Figure 6.14: Diamond bay cross section

The original IsoTruss design contains isosceles triangles that extruded from the surface of the truss forming pyramids. For ease of manufacturing, the pyramidal extrusion was replaced with an octagonal cross-section. This increases the structure's tensile strength and buckling factor. Each diagonal member of the OctaTruss forms an "X" at an angle of 45 degrees along the circumference of the arm (see Figure 6.15).

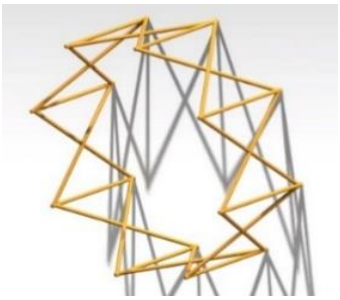

Figure 6.15: "X" bay cross section

The longitudinal and diagonal members of the OctaTruss are epoxy coated carbon fiber composite rods. These rods have a longitudinal Young's Modulus of 120GPa (1.89∃7psi). The longitudinal tensile strength is 1500MPa (2.18∃5psi).

Both sides of the OctaTruss are wrapped with epoxy coated carbon fiber sheets to prevent buckling at points of load transmission. This carbon fiber composite sheet has a longitudinal Young's Modulus of 70GPa (1.02∃7psi) and a longitudinal tensile strength of 600MPa (8.7∃4psi). These wrapped ends of the OctaTruss will then be epoxied inside aluminum caps. These end caps contain the mounting holes for attaching the arm to the cockpit and landing gear assembly (see Figure 6.5 and Figure 6.19). The bolts will be fed through these holes and mate with nuts welded to the cockpit and landing gear assembly.

6.3.1 OctaTruss Structural Analysis

The design of the OctaTruss was determined through a parametric study. The study analyzed how different cross-sectional shapes and bay lengths impacted weight and tip deflection. The bay length is defined by the horizontal distance between each standard "X" that two diagonal members form.

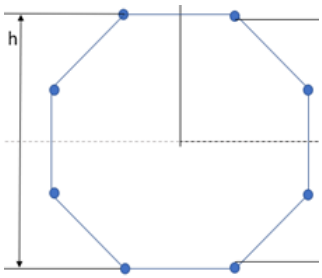

Figure 6.16: Section view of OctaTruss structure

The study began by comparing a hexagonal to an octagonal cross section. When applying a fourth of the gross weight to the tip of the beam while constraining the other end, the octagonal cross section produced better tensile and buckling safety factors. Finite element analysis (FEA) revealed that an octagonal cross-section not only provides better structural integrity, but also weighs less than a hexagonal cross-section for any height (h) (see Figure 6.16).

Samara's first OctaTruss iteration was a 58-bay truss with a height of 25.4cm (10in) and a diamond bay cross section (see Figure 6.11). Each longitudinal and diagonal member had a 0.508cm (0.2in) diameter. While this configuration yielded adequate factors of safety in bending and buckling, the Samara Team desired a lower weight. To minimize weight but maintain structural integrity, the OctaTruss was modified. The new design had a longer bay length with a "X" bay cross section (shown in Figure 6.15).

In order to preserve an octagonal cross section and create a 45 degree "X" with its diagonal members, the OctaTruss could not exceed a bay length of 12.7cm (5in). This resulted in a 28- bay OctaTruss with a

diameter of 33cm (13in). By changing the configuration of the bay cross section, the weight of a 2 m (6.59ft) arm was reduced from 4.76kg (10.5lbs) to 2.81kg (6.2lb). Determined by FEA, the tensile safety factor increased from 7.20 to 9.42 and the max buckling load increased from 3.14∃7N (7.06∃6lb) to 3.17∃7N (7.13∃6lb) producing a buckling safety factor of 9.81∃3. The tip deflection of the OctaTruss was calculated by applying the rotor thrust (25 % of the gross weight) to the tip of the OctaTruss in the positive Y direction while fixing the end. ANSYS found that

a 2m (6.59ft) long OctaTruss has a 7.37mm (0.29in) tip deflection (see Figure 6.17). The tip deflection is less than 2% of the total length of the beam and is an indication of the high bending stiffness of the structure. This high stiffness results in higher than usual factors of safety. It has a tensile safety factor of 8.10 given that the max equivalent stress in the OctaTruss is 182.9 MPa (2.653∃4psi) (see Figure 6.18) and the yield tensile strength for the carbon fiber is 1.503GPa (2.18∃5psi). Note the actual tip load will be less than the rotor thrust because of the presence of the battery, gear box, and motor. Therefore, the tip deflection will be lower than 0.29 inches. This results in an even higher factor of safety.

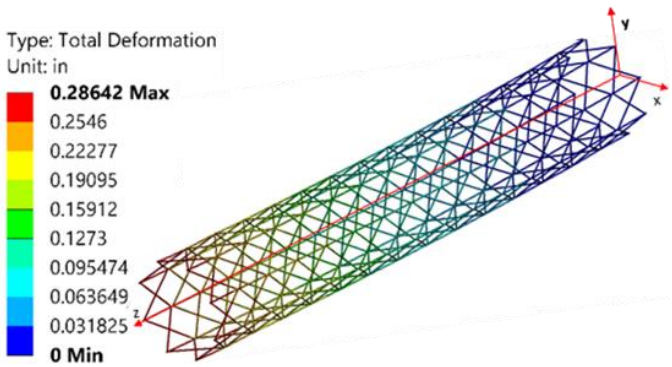

Figure 6.17: OctaTruss tip load deflection

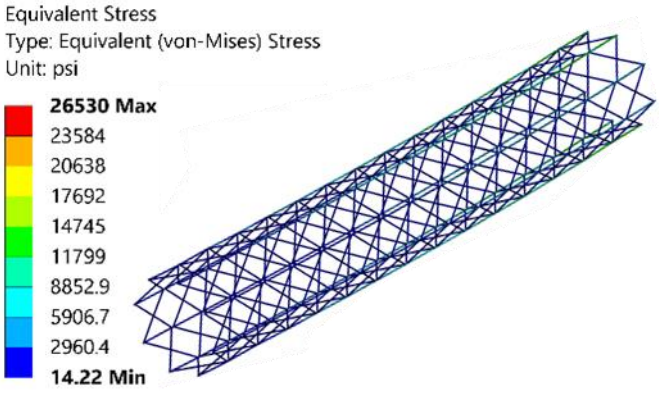

Figure 6.18: OctaTruss equivalent stress response

6.4 Cockpit

The cockpit is the central hub for *Samara's* structure. This is to keep the center of gravity low and centralized. The OctaTruss arms connect to a lightweight carbon fiber structure below the pilot's seat. This hub also functions as a footrest.

The seat is constructed out of Styrofoam, with a canvas backrest, and is supported by rubber shock absorbers. The cockpit is equipped with a crisscross restraint. and positions the pilot so they have a clear view of the flight path with no obstruction from the rotors. The cockpit is inspired by Lift Aircraft's *Hexa* vehicle [12].

The cockpit is designed for the 50th percentile male. It is a 1.3cm (0.5inch) solid carbon fiber shell offering a lightweight structure while ensuring pilot safety throughout the flight. Its windshield is a 5.1mm (0.2in) thick acrylic sheet to protect the pilot from wind, weather, and debris. Below the pilot's seat is a cylindrical hub that is used for connection of the OctaTruss arms.

Figure 6.19: Cockpit

Below the pilot's seat is a cylindrical hub that is used for connection of the OctaTruss arms. In the center of the hub is a 0.36m (14in) diameter storage compartment that houses the avionics equipment. Each

OctaTruss arm is connected at a 45-degree angle from the pilot's forward direction. Each arm is connected by an aluminum collar.

6.4.1 Cockpit Structural Analysis

Figure 6.21 and Figure 6.20 illustrate the deformation and equivalent stress when 2.39kN (537lb) vertical force is applied. The frame has a significant safety factor. The max stress occurs on the outer edges of the top surface of the cockpit frame. The carbon fiber sheet has a longitudinal Young's Modulus of 70GPa (1.02∃7psi). The longitudinal tensile strength is 600MPa (8.70∃4psi).

The acrylic windshield is designed to withstand a 1kg (2.2lb) bird strike for a vehicle traveling at 26.8m/s (52knots). Acrylic has high impact resistance, high optical clarity, innate weatherability, UV resistant, and light weight. It as a Young's Modulus 2.5GPa (3.63∃5psi) and a tensile strength of 60 MPa (8.7∃3psi). Figure 6.19 and Figure 6.19 (on Page 2) illustrate the resulting deflection and equivalent stress from a bird strike.

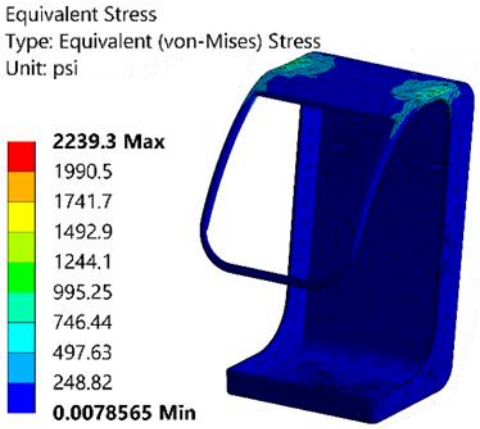

Figure 6.20: Cockpit stress response

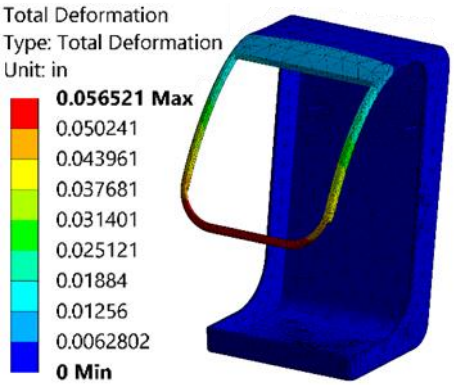

Figure 6.21: Cockpit frame deformation

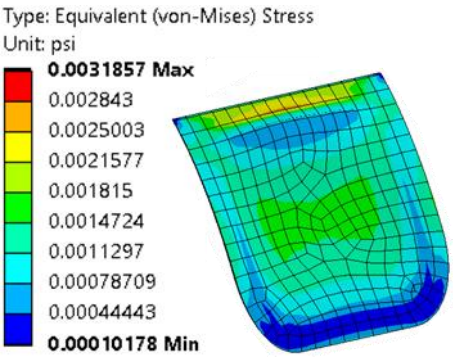

Figure 6.22: Windshield stress response due to bird strike

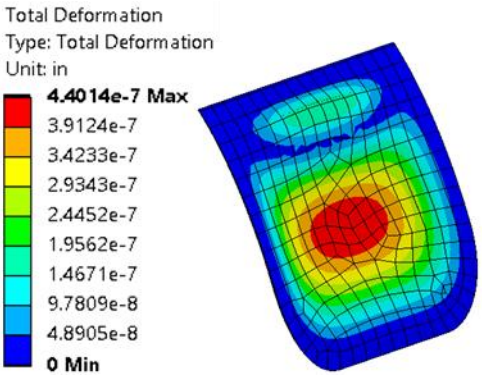

Figure 6.23: Windshield deformation due to bird strike

Table 6.1:
Motor, Gearbox, and Landing Gear Assembly Dimenstions

Parameter	Value (Metric)	Value (Imperial)
Gearbox diameter	1.740m	5.709ft
Gearbox height	1.380m	4.528ft
Enclosure diameter	0.203m	0.667ft
Enclosure height	0.406m	1.333ft
Enclosure thickness	12.7mm	0.5in
Battery support height	7.2cm	0.236ft
Battery support width	5.9cm	0.194ft
Battery supports length	0.152m	0.499ft
Half sphere shock absorber diameter	0.203m	8in
Damping cylinder diameter	2.54cm	1.0in
Damping cylinder height	2.31cm	0.91in
Stabilization I-beam width	40mm	1.57in
Stabilization I-beam height	30mm	1.81in
Stabilization I-beam length	0.345m	1.13ft
Stabilization I-beam flange thickness	2.5mm	0.1in
Stabilization rod diameter	2cm	0.787in
Stabilization rod length	0.6m	1.969ft
Stabilization rod thickness	2.489mm	0.098 in

Table 6.2: Summary of vehicle specifications

	Parameter	Value (Metric)	Value (Imperial)
Rotor	Base diameter	3.048m	10ft
	Tip diameter	1.59m	5.21ft
	Lifting surface	4.99m^2	53.73ft^2
	Sweep angle	20°	20°
	Solidity	1.191	1.191
	Height	2.05m	6.73ft
	Spar diameter	12.7mm	0.5in
	Spar angular offset	45°	45°
	Spar vertical offset	0.25m	9.84in
	Shaft outer diameter	2.54cm	1in
	Shaft thickness	0.25cm	0.1in
Arm	Isotruss diameter	0.327m	1.0ft
	Longitudinal member diameter	0.508cm	0.2in
Cockpit	Height	1.016m	3.333ft
	Width	0.61m	2ft
	Length	0.778m	2.552ft
	Ground Clearance	5.146m	5.145in
	Windshield thickness	5.1mm	0.2in
	Shell thickness	1.3cm	0.5in

6.5 OctraTruss Mounting Bolts to Cockpit Structural Analysis

A steel bolt with a body length of 25mm (0.98in) is designed to withstand shear forces from the rotor's thrust and axial tension from bending moments in the OctaTruss arm. Since there are four bolts, the shear force on each bolt is the rotor thrust divide by four (178N) and acts in the negative X direction. The axial force is the bending moment divided by two times the distance to the elastic axis (23.82kN) and acts in the positive Z direction. Figure 6.24 and Figure 6.25 show the equivalent shear and tensile stress for a steel bolt with an 18mm (0.71in) head diameter and a 15mm (0.60in) body diameter. The shear strength for 1065 Carbon Steel is 345MPa (5Ǝ4psi). The tensile yield strength is 490MPa (7.11Ǝ4psi). The bolt has a shear safety factor of 27.06 and a tensile safety factor of 8.89.

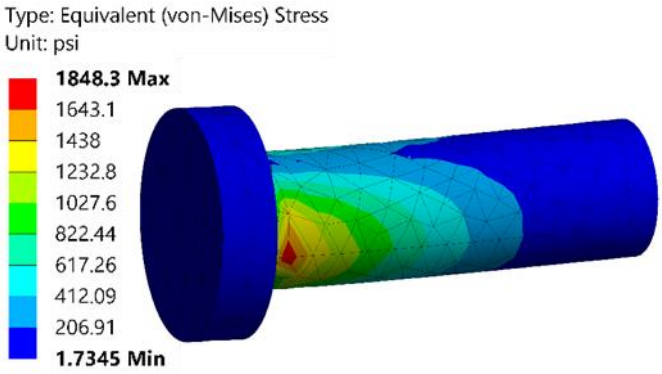

Figure 6.24: Shear stress respose

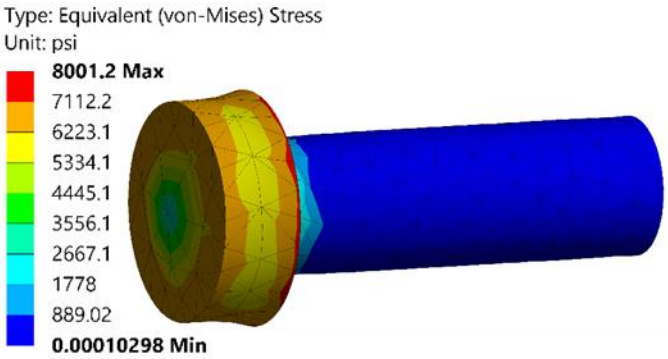

Figure 6.25: Tensile stress respose

6.6 Human Accessibility Factor

Special care has been taken to provide easy access to every component of the powertrain for ease of maintenance through the provision of access hatches. The landing gear has been designed for ease of field repair in case damage. Similarly, minor damages to the four octa trusses can be repaired in situ. In case of more severe damage, they can be removed and replaced on the field.

6.7 Demonstrator Manufacturing and Feasibility

Samara is designed with the intention of quick repairs and easy disassembly for transportation purposes. In achieve this capability, each component of *Samara* was fabricated with manufacturability in mind. This chapter summarizes the manufacturability of the OctaTruss and the cost of *Samara*.

When it comes to using molds for complex part designs, the process can become costly and time consuming. Fused Deposition Modeling (FDM) Technology simplifies the process by designing soluble mandrel material that can be 3D printed [13]. FDM technology is utilized to produce soluble mandrels that allow long and thin features on a part to be produced without concern of damage. This process is perfect for manufacturing the OctaTruss.

The truss is designed in a 3D CAD system and then printed in a soluble material. When the build is complete, the OctaTruss is removed from the system and support structures are detached. The longitudinal members are placed in prepositioned slots and then wrapped in carbon fiber tows. It is then cured at a temperature below 93.3°C (200°F) and at a pressure less than 621kPa (90psi). After curing, the OctaTruss is washed in a solution that removes the soluble material. The ends of the OctaTruss are then epoxied to aluminum end caps so they can be connected to the cockpit and the pylon.

6.8 Cost of Materials

Table 6.3: Estimate cost

Component	Parts	Unit Cost	Quantity	Total Cost
OctaTruss	Carbon Fiber Rods	$1.75/ft	192ft	$ 336.00
	Tows	$0.48/ft	552ft	$ 264.96
	Epoxy	$20/lb	25lb	$ 500.00
	Right Angle Drill Adapter	$96/unit	1	$ 96.00
Rotor	Carbon Fiber Rods	$1.75/ft	6.64ft	$ 11.62
	Unidirectional Carbon Fiber Sheet	$4.40/ft	13ft	$ 57.20
	Epoxy	$20/lb	40lb	$ 800.00
	Dacron	$6/ft^2	53.73ft^2	$ 322.38
Cockpit	Styrofoam	$0.20/lb	0.75lb	$ 0.15
	iPad	$1,000/unit	2	$ 2,000.00
	Plexiglass	$6.78/ft^2	3.6ft^2	$ 24.40
Powertrain	Motor	$2000 estimate	4	$ 8000.00
	Battery	$650	8	$ 5199.92
	Wires	$1.10/ft	32 ft	$ 35.20
	ESC	$134.00 estimate	4	$ 536.00
	Power Module	$25.20	8	$ 201.60
Avionics	The Cube-Pixhawk 2.1	$250/unit	1	$ 250.00
	GNSS	$95/unit	2	$ 190.00
	MB1240 Sonar	$39.95/unit	4	$ 159.90
	QRD1114 Tachometer	$0.63/unit	4	$ 2.52
	Ni1000SOT (Temperature sensor)	$0.78/unit	8	$ 6.24
	mvBlueFox3-4:	$50/unit	5	$ 250.00
	MV-O-SMOUNT 05.0	$180/unit	4	$ 720.00
	MV-O0184-5M-FU	$130/unit	1	$ 130.00
Landing Gear	Sorbothane	$500/mold	4	$ 2,000.00
	Aluminum I-beams	$0.45/lb	2.94lb	$ 1.32
			Total	**$ 22,095.41**

7 Power and Energy

7.1 Powertrain Selection

There are many options when selecting a rotorcraft powertrain. To create an efficient and effective design, it is important to minimize the weight of the powertrain while still providing enough power for the craft to maneuver and perform its mission.

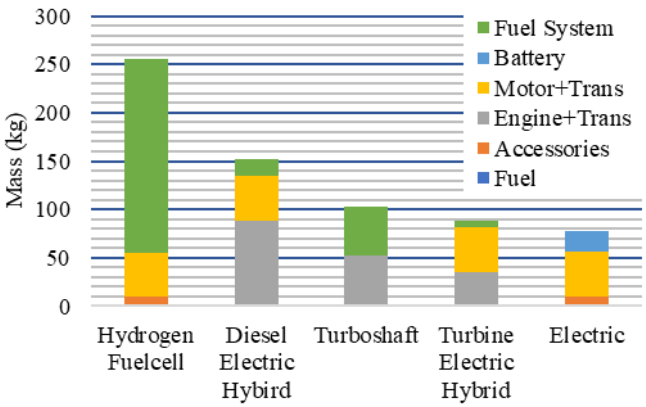

Figure 7.1: Weight estimates of various powertrains

The theoretical powertrain weights of a turboshaft, battery electric, diesel hybrid, turbine electric and hydrogen fuel cell craft were calculated. The results of these calculations can be seen in Figure 7.1. All powertrains can provide 100kW of power for a period of 120 seconds. The lightest solution is a 77kg (170lb) battery-electric powertrain. The second lightest is an 88kg (194lb) turbine electric system by.

A battery electric powertrain is efficient, with the only disadvantage is battery have less energy density compared to hydrocarbon fuel. This disadvantage is mitigated by the brevity of the flight plan outlined in the RFP. Therefore, a fully electric powertrain was selected for the design.

7.2 Power Requirements

The sizing code in Chapter 3.1 estimates the power draw of *Samara* in hover to be 55kW. Therefore, each motor must operate with at least 13.75kW of power. The angular velocity of the rotors in hover was also determined to be 340 RPM. To keep the transmission compact, no more than 2 stages should be used – a maximum of 16:1 output reduction was mandated. This results in a hover operating RPM of 5440.

7.3 Powertrain Components

7.3.1 Motor

Both Alternating Current (AC) and Direct Current (DC) motors were considered for this design. To use DC batteries to power an AC motor. an inverter must be added to the circuit; this increases complexity and weight. Subsequently, AC motors are more expensive to install.

DC motors may operate at higher voltages than they are rated for short periods of time, to produce more power, useful for short, rapid maneuvers. Furthermore, AC motors only use current to produce a rotating

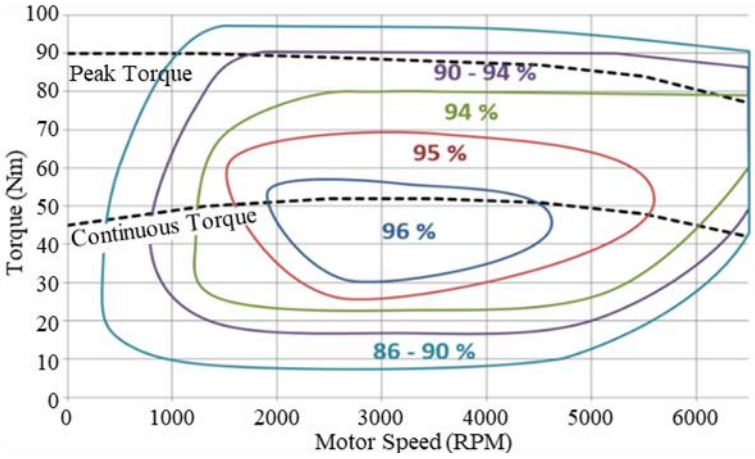

Figure 7.2: EMRAX 188 combined cooling efficiency chart

magnetic field to spin the rotor, while DC motors also depend on magnets. This means that DC motors are slightly more efficient, however they cannot produce as much peak power. Ultimately, the power requirements of *Samara* are well within the limits of DC technology, so a DC motor was selected.

No existing motor designed for aeronautical applications capable of providing approximately 15kW of power exists on the market. That power level is above typical heavy-lift drone motors but is below manned aircraft motors.

A theoretical motor, with performance equal to current motor technology, was devised for this application. The scaled motor is based on the EMRAX product line. Their smallest, the 188, produces 22kW to the 15kW that is required for Samara. It is too heavy for this application. It is also inefficient (>90%) when outputting 25Nm of torque at 5440rpm, Samara's hover state (see Figure 7.2). The figure shows that efficiency increases at maximum torque. Therefore, a smaller motor would itself weigh less, and decrease battery weight.

In order to determine the maximum operating RPM of the scaled motor, the values for the three weakest EMRAX motors were plotted as functions of their continuous power rating Figure 7.3. A polynomial regression was used to determine that a motor with 15kW of continuous power draw would have a maximum operating RPM of 7000.

Each EMRAX motor has three distinct operating profiles, high, medium, and low voltage. A similar profile was desired for the scaled motor. A polynomial regression of voltages for each motor was utilized. From known voltages and RPM, the voltage constant (Kv) (a metric that relates the voltage the motor receives to the RPM at which it spins) could be calculated for high, medium, and

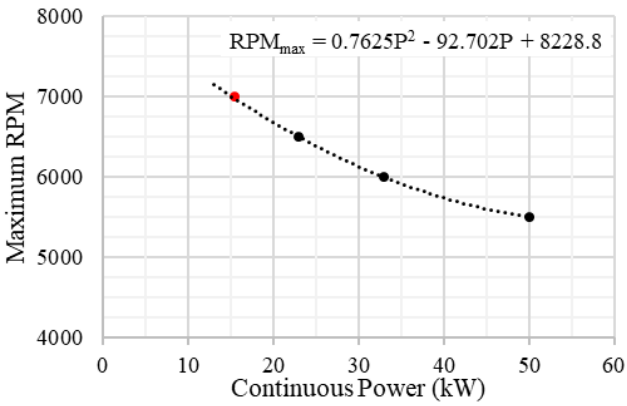

Figure 7.3: Maximum RPM as a function of continuous power

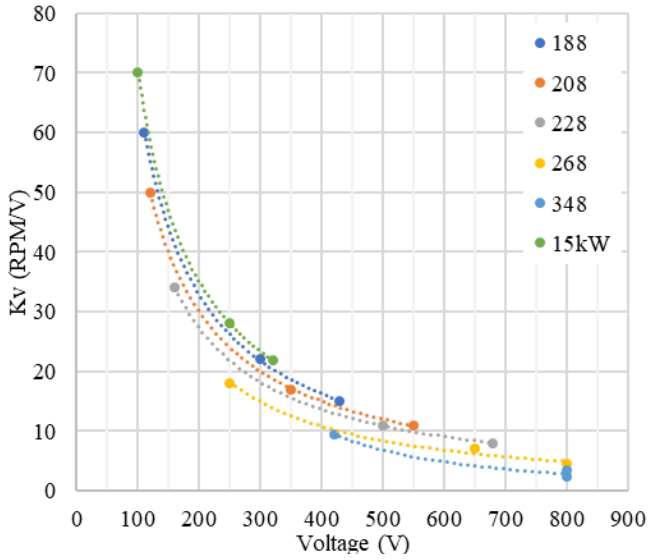

Figure 7.4: Kv as a function of voltage of EMRAX motors

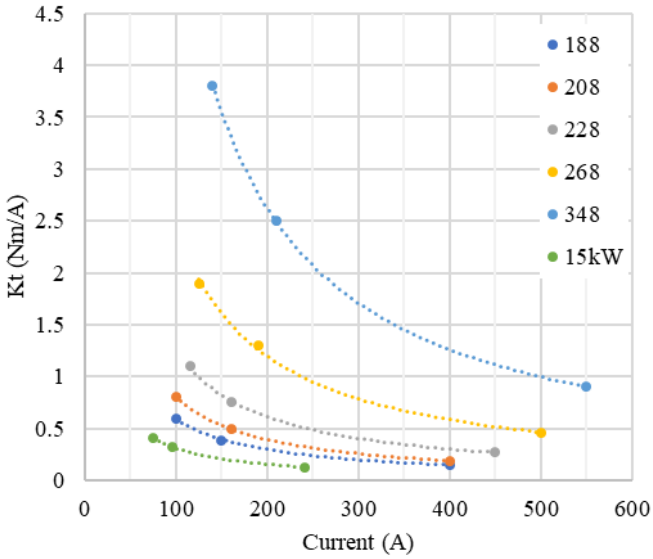

Figure 7.5: Kt vs. current of EMRAX motors

low voltages. Each EMRAX motor constant and the scaled motor is plotted as a function of voltage, to show agreement in shape and trends as motor size decreases (see Figure 7.4). The maximum current was calculated using the three voltages and the motors' rated continuous power. From these values the torque constant (Kt), was calculated and plotted against current for each motor to show agreement between the existing EMRAX motors and the theoretical values (see Figure 7.6). Kt is also a characteristic of the motor, and it relates the current seen by a motor to the amount of torque it outputs.

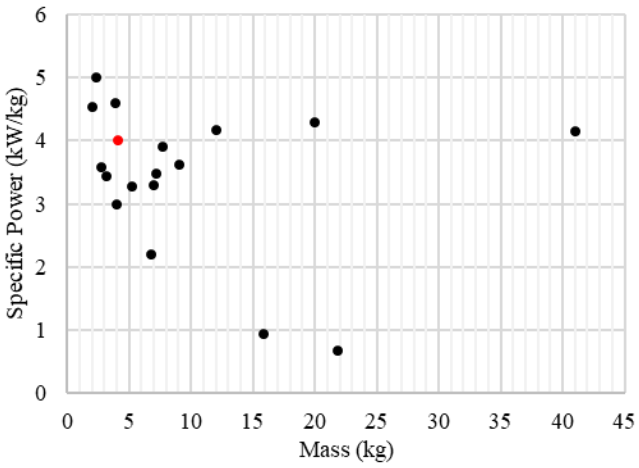

Figure 7.6: Specific power vs. mass of EMRAX motors

With the motor constants for each operating mode calculated, the proper operating voltages and currents were determined for high, medium and low voltage situations (see Table 7.1). These are the voltages and currents which would give the proper power to the rotor in each operating mode. The final determination of the operating voltages and currents were determined by the battery and ESC specifications, as they proved to be the limiting factor. The final scaled motor was calculated to produce a maximum of 16.6kW continuous power but is limited to 15kW in this application.

Table 7.1: Kt and Kv Values for Operating Voltages

Voltage Profile	Kv (RPM/V)	Kt (Nm/A)	Voltage (V)	Current (A)
High	21.9	0.415	320	75.4
Medium	28	0.324	250	96.5
Low	70	0.13	100	241.1

The motor is estimated to weigh 4.15kg (9.13lb), at a specific power of 4kW/kg. This value for specific power was arrived at by compiling the specific powers of motors on the market. Although there were motors available with higher specific powers, 4 kW/kg was used as a conservative value. A plot of these values, along with the scaled motor indicated in orange, can be seen in Figure 7.6.

7.3.2 Battery

Several battery options were considered. A custom battery pack could be constructed from individual cells, or one or more existing battery packs could be wired into the circuit. To determine the ideal battery configuration, a parametric study was conducted to calculate the minimum weight for a battery which met voltage, current and capacity requirements. Table 7.2 shows several products which were considered.

C rate relates battery capacity to maximum output voltage. Since this application has a relatively small battery capacity due to the short flight profile, but still has high current requirements, a C rate of at least 24 was needed to provide adequate current without carrying extra capacitance. The minimum battery weight was determined to be 4.68kg (10.3lb) per motor totaling to 18.72kg (41.18lb). This configuration has enough capacity for a 183s endurance – over 3 times the RFP required minimum. The battery packs consist of 2 Max Amps Li-Po 9000xl 12s battery packs wired in series (see Figure 7.8). This set-up provides 9000mAh to each motor and can supply a maximum of 88.8V and 900A. The motors in hover require 77.7V and 177A.

Table 7.2: Comparison of Battery Weights Required to Meet Vehicle Specifications

	Required Values	Samsung 40T	Samsung 25R	Max Amps Li-Po 3250	Max Amps Li-Po 9000XL	Turnigy LiPo	Tattu 3S1p	Sony VTC3	VapCell INR	Lumenier JST-PH 2.0
Voltage (V)	77.7	79.2	77.7	88.8	88.8	77.7	77.7	79.2	79.2	77.7
Current (A)	193	201.25	200	1462.5	900	450	414	180	190	205
Total # of Cells	-	2024	336	24	8	56	112	528	440	3360
Total Weight (kg)	18.2 Desired	135	94.5	22.8	18.7	25.5	20.0	23.8	21.1	20.5
Total Capacity (Ah)	32.17	92	100	39	36	40	36.8	38.4	40	32.8

7.3.3 Electronic Speed Controller

The low voltage high current operating mode is would normally be inefficient due to the high current draw and resultant losses in wiring. However, since the ESSC is mounted adjacent to the batteries, wire resistance is negligible, resulting in minimal operating losses. Operating in this mode enables the utilization of the lightest battery configuration and availability to use a commonly available ESC. Akin to the motors, the operating window of the ESC lies between light and heavy duty; most ESCs within the weight requirements can operate either on the required voltage or the required current, but not both. An AMPX ESC 200A(12s-24s) HV is used in this application, and as it is rated to 200A of continuous current. and continuous 100V Figure 7.10. It weighs 0.580 kg (1.276lbs).

7.3.4 Standard Operating Conditions

Table 7.3: Motor: 16.6kW Scaled EMRAX Motor

	Hover	Advertised
Kv (RPM/V)	70	-
Kt (Nm/A)	0.13	-
Voltage (V)	77.7	320
Current (A)	177	241
Power (kW)	13.75	16.6
Torque (Nm)	25.01	25
Weight	4.15kg (9.13lb)	4.15kg (9.13lb)
Efficiency	0.95	0.96
RPM	5440	7000

Figure 7.7: EMRAX 188

Figure 7.8: MaxAmps Li-Po 44.4V 9000XL

Figure 7.9: Mauch HS-200-HV

Figure 7.10: AMPX ESC 200A (12s-24s) HV

Table 7.4: ESC: AMPX ESC 200A (12s-24s) HV

	Hover	Advertised
Power (kW)	13.5	30
Current (A)	177	200
Weight	0.58kg (1.28lb)	0.58 kg (1.28lb)
Voltage (V)	77.7	100

7.3.5 Powertrain Circuit

Each rotor transmission and motor will be powered by an independent battery pack. These circuits will be self-contained other than the ESC and 2 power modules used to monitor the batteries, which are connected to the central flight controller. The wiring diagram (Figure 7.11) depicts the 4 separate batteries, and the ESCs connected to the flight controller. Layouts utilizing a single battery for the entire craft and individual batteries for each motor were considered. Individual batteries are the superior configuration because it minimizes the length of heavy high-current wire, by dramatically reducing the distance between the batteries and the ESC.

Each individual motor circuit is enumerated in Figure 7.9. Starting in the lower left of the diagram, is a MaxAmps battery. Wired into its positive cable is a Mauch HS-200-HV power module (Figure 7.12). This is also connected to the individual cell voltage outputs from the battery pack. The power module relays battery health and current draw to the flight controller. The module can handle a continuous 200A. Using this data the amount of the battery's capacity which has been depleted can be calculated. The module is rated to a maximum of 60V, well above the 44.4V that the battery outputs. The cell voltage monitor records the voltage remaining in each cell. This allows the flight controller to ensure that battery cells are not being over depleted. This second battery is monitored by a second Mauch unit before sending power to the ESC which is also connected to the flight

Table 7.5: Battery: MaxAmps Li-Po 44.4V 9000XL

	Hover	Installed Unit	Advertised
Capacity (Ah)	8.041	9	9
Voltage (V)	77.7	88	44.4
Current (A)	177	900	900
Weight (kg)	4.68kg (10.3lb)	4.68kg (10.3lb)	2.34kg (5.15lb)
C rate	-	100	100
Total Weight (kg)	18.72kg (41.18lb)	18.72kg (41.18lb)	-
Total Capacity (Ah)	32.17	36	-

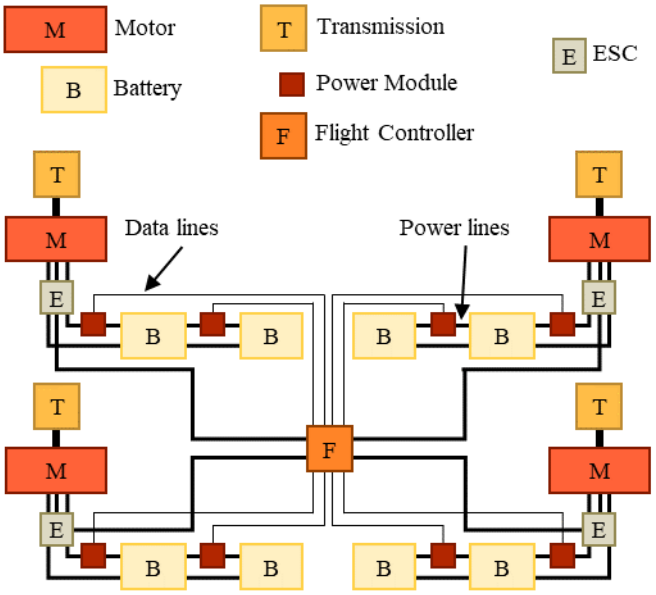

Figure 7.11: Wiring diagram of vehicle powertrain

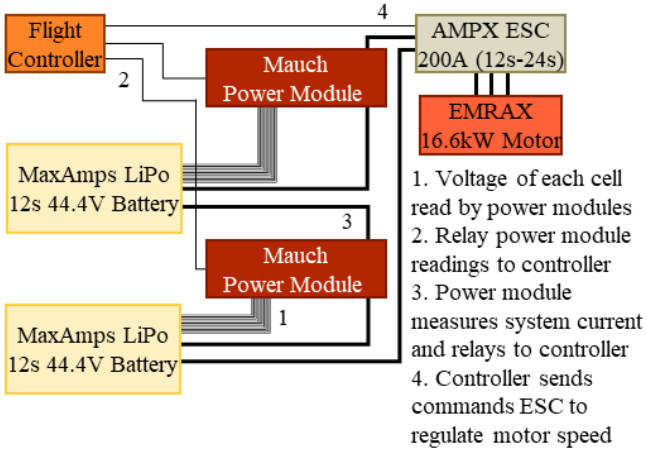

Figure 7.12: Circuit associated with each rotor

controller. The motor is connected to the ESC's 3 leads, and the ESC is wired into the first battery's ground terminal

8 Controls and Piloting

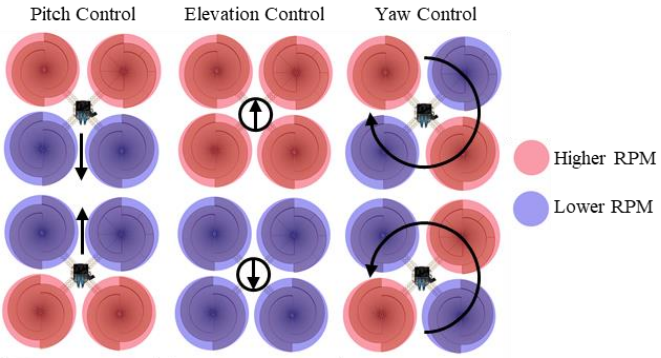

Figure 8.1: Samara RPM control diagram

Samara's avionics and sensors were chosen so that it may complete any mission autonomously or under pilot control. For a quadrotor, control of all nine degrees of freedom is controlled by changing the RPM of the rotors. Elevation can be controlled by increasing and decreasing the RPM of all rotors evenly; RPM directly corresponds to the amount of lift generated by the Aerial Screw Figure 8.1 depicts how the imbalances in rotor RPM allow the Samara to control directional inputs. This allows the vehicle to maneuver in all 9 degrees of freedom by increasing the RPM of the corresponding rotors

For *Samara* to yaw, the RPM of the opposing pair of rotors must be decreased while the other is increased. For *Samara* to pitch forward, the RPM of the front two rotors would be decreased while the RPM of the back two rotors were increased. These simple RPM controls allow *Samara* to maintain a steady elevation while performing maneuvers.

8.1 Mission Avionics Requirements

Samara's avionics were chosen so to enable it to autonomously fulfil any programmed mission profile to reduce the pilot workload. *Samara* is equipped with an inertial measurement unit (IMU), an ultrasonic sensor, cameras, and a processor to collect the data measured by the sensor array. The complete avionics package includes: The Cube Pixhawk 2.1, Here 2 GNSS for Pixhawk 2.1 Module, and the MB1240 ultrasonic sensor – with supporting avionics, Ni1000SOT thermistors, mvBlueFox3-4 camera, and MV-O-SMOUNT 05.0, and MV-O01814-5M-FU lenses (see Figure 8.3). Sensor readings throughout the mission are listed in Table 8.1.

Figure 8.3: Onboard avionics

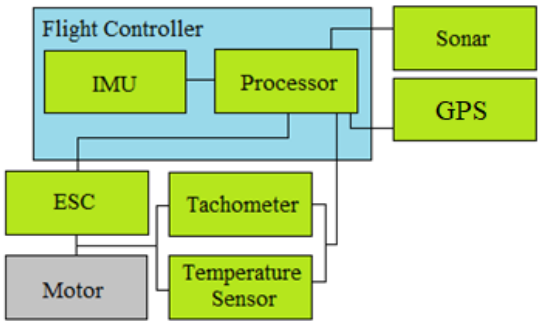

Figure 8.2: Control system concept flow chart

Table 8.1: Sensor readings throughout mission

Operation	Task	Active Sensor
Entire Mission	Send commands to flight controller, display sensor readings for pilot	iPad
	Collect data from sensor array, send commands to powertrain – Figure 8.2 illustrates control system processes	"Pixhawk 2.1 – The Cube" IMU: flight controller
	Feedback rotor RPMs to flight controller	"QRD1114" (Tachometer)
	Monitor battery, ESC, and motor temperatures	Thermistors
Pre-flight	Evaluate avionic and powertrain system health by conducting a full system diagnostic	Pixhawk
	Display full system health	iPad
	Program mission profile	iPad
Take-off and Landing	Determine if *Samara* is grounded – measure altitude	"MB1240 XL-MaxSonar-EZ4" (Sonar)
	Maintain level ascent and descent – track 9 axis motion	Pixhawk
	Ensure direct vertical ascent and descent – track GPS position	"Here 2 GNSS Module" (GPS): GPS position
Hover	Maintain 1m (3.3ft) altitude – measure altitude	Sonar
	Hold position within 10m radius of take-off and landing spot – track GPS position	GPS
	Redundant confirmation of position hold – track 9 axis motion	Pixhawk
Forward Flight	Increase rear rotor RPM and decrease forward rotor RPM to pitch *Samara* forward and initiate forward flight	Pixhawk
	Time forward flight to meet mission requirements	Pixhawk
	Maintain 1m (3.3ft) altitude – measure altitude	Sonar
	Use Earth's gravitational field to maintain heading	Pixhawk
	Redundant confirmation of heading – track GPS position	GPS
	Decrease rear rotor RPM and increase forward rotor RPM to pitch *Samara* backwards and stop forward flight	Pixhawk

Table 8.1: Avionic component description

Component	Description
The Cube – Pixhawk 2.1	Flight controller with 32-bit processor that interfaces with sensor array. Utilizes the two external GPS modules, by linking both receivers and blending the data using an algorithm within the Estimation and Control Library of the Cube to increase position precision. Embedded IMU with triple redundant sensor package including three 9 axis, motion tracking IMUs; three accelerometers, gyroscopes, and magnetometers contained within an isolated and damped platform.
Here 2 GNSS Modules	Two GPS modules with embedded magnetometers increase position precision to 0.8m (2.62ft).
MB1240 XL-MaxSonar-EZ4	Narrow beam sweep for considerable noise reduction with 1cm (0.39in) precision and 0.2m (7.87in) to 7.65m (25.1ft) range.
mvBlueFox3-4	Five high resolution camera that increases pilot's visibility by over 500%. Cameras are mounted to each of the landing gear assemblies and one is mounted beneath the cockpit giving them a full panoramic view of *Samara's* surroundings.
MV-O-SMOUNT 05.0	Four wide view lenses with 5mm (0.2in) focal length and a horizontal Field Of View (FOV) of 87° attached to each of the landing gear assembly cameras – to increase camera field of view.
MV-O01814-5M-FU	185° FOV fisheye lens is mounted to the camera beneath the cockpit, enabling the pilot to conduct safe, unobstructed, landings.

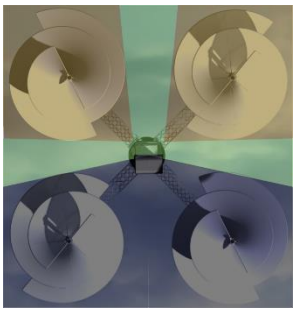

Figure 8.4: Top-down view of pilot sightlines
green regions: unobstructed FOV
yellow regions: FOV obstructed by rotors
gray regions: FOV obstructed by cockpit

Figure 8.5: Pilot point-of-view FOV, 18% is unobstructed, cameras increase pilot FOV by over 500%

8.1.1 Cockpit Display and Controls

Samara's cockpit display was designed with safety and usability in mind (see Figure 8.6). The displays span across two iPad Pros accumulating to 603 cm^2 (93.4in^2) of screen. The features of the UI are listed below:

Full panoramic view of *Samara's* surroundings, eliminating the blind spots caused by the rotors (see Figure 8.4 and Figure 8.5).

Mission profile interface to see current stage of flight, and program missions

Pilot controls for manual control of yaw, pitch, and roll

Powertrain temperature readings allow the pilot to monitor component health and eliminate the risk of overheating

Four-point altimeter readings show the altitude of each landing gear assembly for easy landings

Compass with airspeed to maintain straight flight and speed

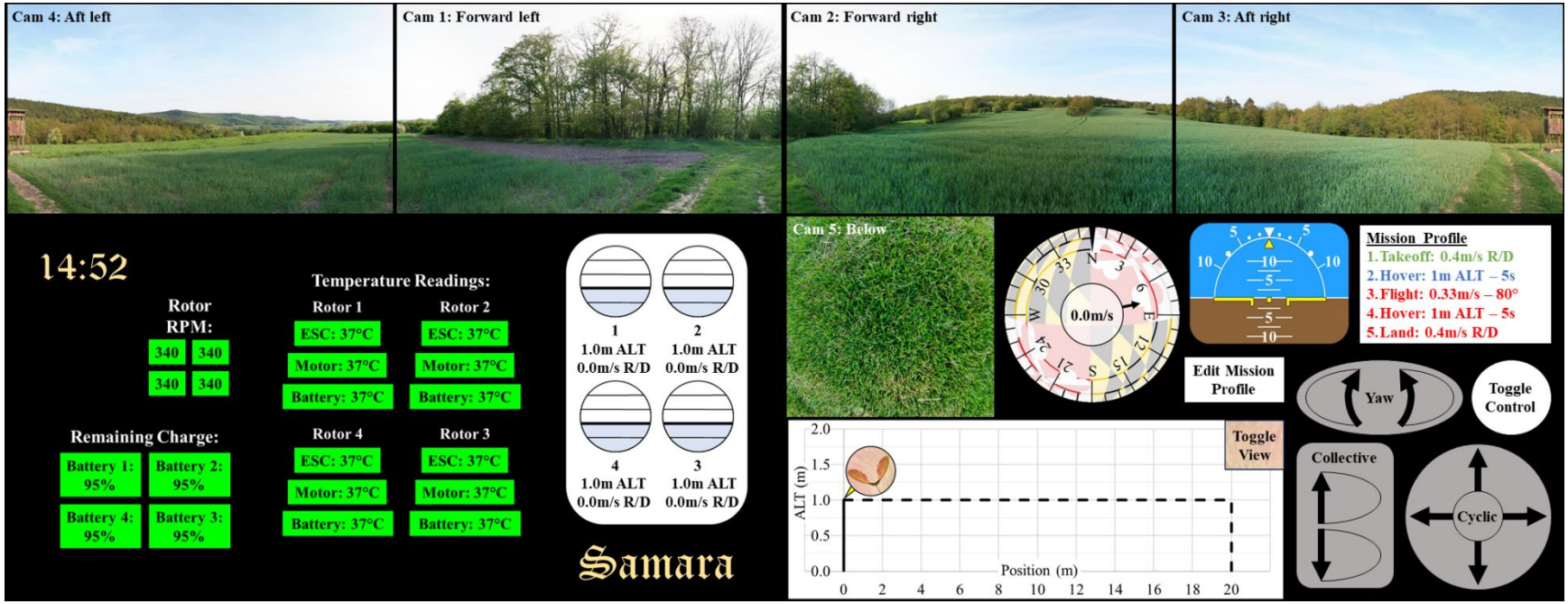

Figure 8.6: Cockpit Display and Controls

9 Capability, Performance, and Requirement Compliance

Table 9.1: *Samara* RFP Requirements and Compliance

RFP Requirement	Solution	Chapter
The rotorcraft must rely on one or more single-blade rotors with solidity equal or greater than one with a continuous surface.	Samara utilizes four Aerial Screws for lift and thrust.	[4], [6.1]
The rotorcraft must be capable of transporting a human load of 60kg (132lb).	Samara has the capacity to transport a 60kg (132lb) Capable of transporting an additional payload of 95kg (209lb).	[5.12], [7]
The rotorcraft must be capable of executing the following mission: Vertical takeoff to altitude of 1m (3.3ft). Maintain position within 10m (33ft) of take-off spot for 5sec. Flight for at least 60sec, covering at least 20m (66ft) distance at an altitude of at least 1m (3.3ft), untethered. Vertical landing, after holding position for 5sec within 10m (33ft) of landing spot.	Samara's flight control system enables it to maintain position with a 0.8m (2.62ft) precision utilizing dual GPS technology. *Samara* exceeds the 70sec endurance and 20m (66ft) requirements. Capable of 183sec hover. Samara operates autonomously. Mission profiles are programmed into the flight control system.	[3], [5.12], [7], [8]

Table 9.2: Documentation Requirements and Compliance

Documentation Requirement	Chapter
Concept definition and description	[1.1], [3]
Configuration trade off analysis	[2]
Preliminary study of all required systems including aerodynamics, structures, powerplant, rotor, controls, based on documented existing proven technologies and existing equipment	[4.4.6], [4.5], [4.6], [5], [6], [6.1], [6.2], [6.3], [6.4], [7], [8]
Preliminary capability and performance definition	[3], [4], [5.12], [7]
Validation of the design and aircraft elements, especially as far as the Aerial Screw lifting devices, by analysis, simulation, or scaled models	[4], [5]

Bibliography

[1] "Leonardo da Vinci," History.com, 21 February 2020. [Online]. Available: https://www.history.com/topics/renaissance/leonardo-da-vinci. [Accessed 8 May 2020].

[2] Vertical Flight Society, 8 September 2019. [Online]. Available: https://vtol.org/files/dmfile/leonardo-rfp_-vfs-sdc-2019_final. [Accessed 13 September 2019].

[3] G. Leishman, Principles of Helicopter Aerodynamics, New York: Cambridge University Press, 2000.

[4] "Doing DaVinci," Discovery Channel, 16 August 2010. [Online]. Available: https://en.wikipedia.org/wiki/Doing_DaVinci#cite_note-MSN-5. [Accessed 8 May 2020].

[5] A. Jeffries, "Cove Collective," The Central Online Victorian Educator, 22 May 2019. [Online]. Available: https://editions.covecollective.org/content/leonardo-da-vincis-aerial-screw. [Accessed 18 May 2020].

[6] Aircraft Sprice and Speciality Company, [Online]. Available: https://www.aircraftspruce.com/catalog/cmpages/peelply4.php. [Accessed 18 May 2020].

[7] NASA, "Open-Lattice Composite Design Strengthens Structures," [Online]. Available: https://spinoff.nasa.gov/Spinoff2007/ip_1.html. [Accessed 18 May 2020].

[8] M. Ramasamy, B. Johnson and G. J. Leishman, "Understanding the Aerodynamic Efficiency of a Hovering Micro-Rotor," *American Helicopter Society,* vol. 53, no. 412, p. 20, 2008.

[9] J.-A. Faust, Y. S. Jung, J. Baeder and J. Rauleder, "Aerodynamic Analysis of an Asymmetric Lift-Offset Compound Helicopter inForward Flight using the Mercury CFD Framework," Alfred Gessow Rotorcraft Center at the University of Maryland, College Park, 2020.

[10] "Sorbothane Performance Curves," Sorbothane, 2015. [Online]. Available: https://www.sorbothane.com/Data/Sites/31/pdfs/data-sheets/102-Sorbothane-performance-curves.pdf. [Accessed 20 May 2020].

[11] "Sorbothane Overview," Sorbothane, [Online]. Available: https://www.sorbothane.com/material-properties.aspx. [Accessed 20 May 2020].

[12] D. Coldewey, "Lift Aircraft's Hexa may be your first multirotor drone ride," TechCrunch, 11 December 2018. [Online]. Available: https://techcrunch.com/2018/12/11/lift-aircrafts-hexa-may-be-your-first-multirotor-drone-ride/. [Accessed 23 May 2020].

[13] J. Hanssen, "Composite Soluble Mandrel Tooling," Stratasys, 2020. [Online]. Available: https://www.stratasys.com/fdm-technology. [Accessed 25 May 2020].

[14] L. d. Vinci, "Study for an Aerial Screw," 29 March 2005. [Online]. Available: https://contentdm.lib.byu.edu/digital/collection/Civilization/id/740/. [Accessed 8 May 2020].

[17] "Material Properties of Sorbothane," Sorbothane, 2018. [Online]. Available: https://www.sorbothane.com/Data/Sites/31/pdfs/data-sheets/101-sorbothane-material-properties.pdf. [Accessed 20 May 2020].